



Kirigami Engineering: The Interplay Between Geometry and Mechanics

Xiangxin Dang

Department of Civil and Environmental
Engineering,
Princeton University,
Princeton, NJ 08544
e-mail: xd7191@princeton.edu

Glaucio H. Paulino¹

Fellow ASME
Department of Civil and Environmental
Engineering,
Princeton Materials Institute (PMI),
Princeton University,
Princeton, NJ 08544
e-mail: g paulino@princeton.edu

Kirigami, as a scientific concept that emerges with but distinguishes from origami, provides a paradigm for engineering the mechanical properties of a surface through geometric analysis. The cutting geometry pattern that enables panel rotations around shared nodes—by itself or in conjunction with folding geometry that allows panel rotations around shared edges—yields predictable mechanical responses ranging from two-dimensional (2D) to three-dimensional (3D) deformations and from shape-fitting to metamaterial functionalities. This contribution reviews the deterministic relationships between geometry of a kirigami surface and its mechanical responses under given external loading. We highlight rigid and nonrigid 2D deformations determined by the convexity, compatibility, or symmetry of the cutting patterns (e.g., tessellations characterized by wallpaper groups); 3D deformations controlled by cutting distance versus surface thickness, slit shapes, or the combined effect of cuts and folds; and mechanical metamaterial functionalities arising from unique lattice connections and panel orientations, including topological polarization transformation, static nonreciprocity, and Poisson's ratio functional variation. We address various methodologies for linking geometry and mechanics in kirigami surfaces, including theoretical analyses, surrogate modeling, finite element simulations, and experimental evaluations. We also discuss strategies for fabricating kirigami surfaces, such as 3D printing, molding, assembling, cutting, and folding. Finally, we project a vision for the field of kirigami engineering by emphasizing the mechanisms that transform subtle geometric characteristics of kirigami surfaces into their unique mechanical properties.

[DOI: 10.1115/1.4068659]

1 Introduction and Motivation

The mechanical properties of a surface can be precisely engineered by cutting it into a network of interconnected components with intricate geometry. We call this process *kirigami engineering*, the twin of *origami engineering* [1]. Although *kirigami surfaces* can exhibit other distinguishing properties, such as thermal [2] or electromagnetic [3] characteristics, this contribution focuses on the interplay of geometry and mechanics (Fig. 1). Ideally, the distribution of *cuts* determines the two-dimensional (2D) deformations of a kirigami surface. For example, convex cuts often lead to rigid deformations whereas nonconvex cuts result in nonrigid deformations (Fig. 1(a)). On the other hand, the thickness of a kirigami prototype significantly influences its three-dimensional (3D) buckling behavior. Broadly speaking, large thickness generally stabilizes 2D deformations, while small thickness may induce out-of-plane buckling (Fig. 1(b)). Furthermore, the intrinsic geometry of the 2D space where a kirigami surface resides rules its deformation characteristics. Nonzero Gaussian curvature imposes more constraints on the kirigami surface. Thus, nonrigid deformations are typically inevitable in a non-Euclidean space, while rigid deformations can be pursued in a Euclidean space (Fig. 1(c)). Lastly, the unique connectivity within periodic kirigami can give rise to exotic mechanical properties. This is exemplified by the *locally isostatic*

lattice, also known as the *Maxwell lattice*, where the number of connections (i.e., constraints) equals the number of degrees-of-freedom at the unit cell level. Notable instances include the triangular (i.e., kagome) lattice and the square-rhombus lattice (Fig. 1(d)). The kagome lattice is topologically polarized, which concentrates floppy modes on one of its edges and stress-bearing modes on the other edge. The square-rhombus lattice is mechanically nonreciprocal, which breaks the transmission symmetry of a force between two points of the lattice.

In this paper, we review how the geometry of kirigami surfaces governs their mechanics. Here, the “geometry” spans not only the shapes of cuts and panels, cut distributions, intrinsic curvatures, and pattern symmetries, but also practical considerations such as surface thickness and the dimension of living hinges. The resulting “mechanics” include rigid and nonrigid 2D deformations (Sec. 2), 3D deformations involving buckling or folding (Sec. 3), and metamaterial properties such as topological polarization transformation, static nonreciprocity, and varying Poisson’s ratio (Sec. 4).

2 On Two-Dimensional Deformations

Since kirigami engineering is performed on a surface, the most basic deformation mode is the 2D deformation within the surface. In this case, the kirigami hinges only allow the connecting panels to rotate around axes perpendicular to the surface. In theory, the cutting geometry typically determines the deformation mechanics, either rigid (i.e., energy-free) or nonrigid (e.g., monostable or bistable),

¹Corresponding author.

Manuscript received April 14, 2025; final manuscript received May 6, 2025; published online September 24, 2025. Assoc. Editor: Yonggang Huang.

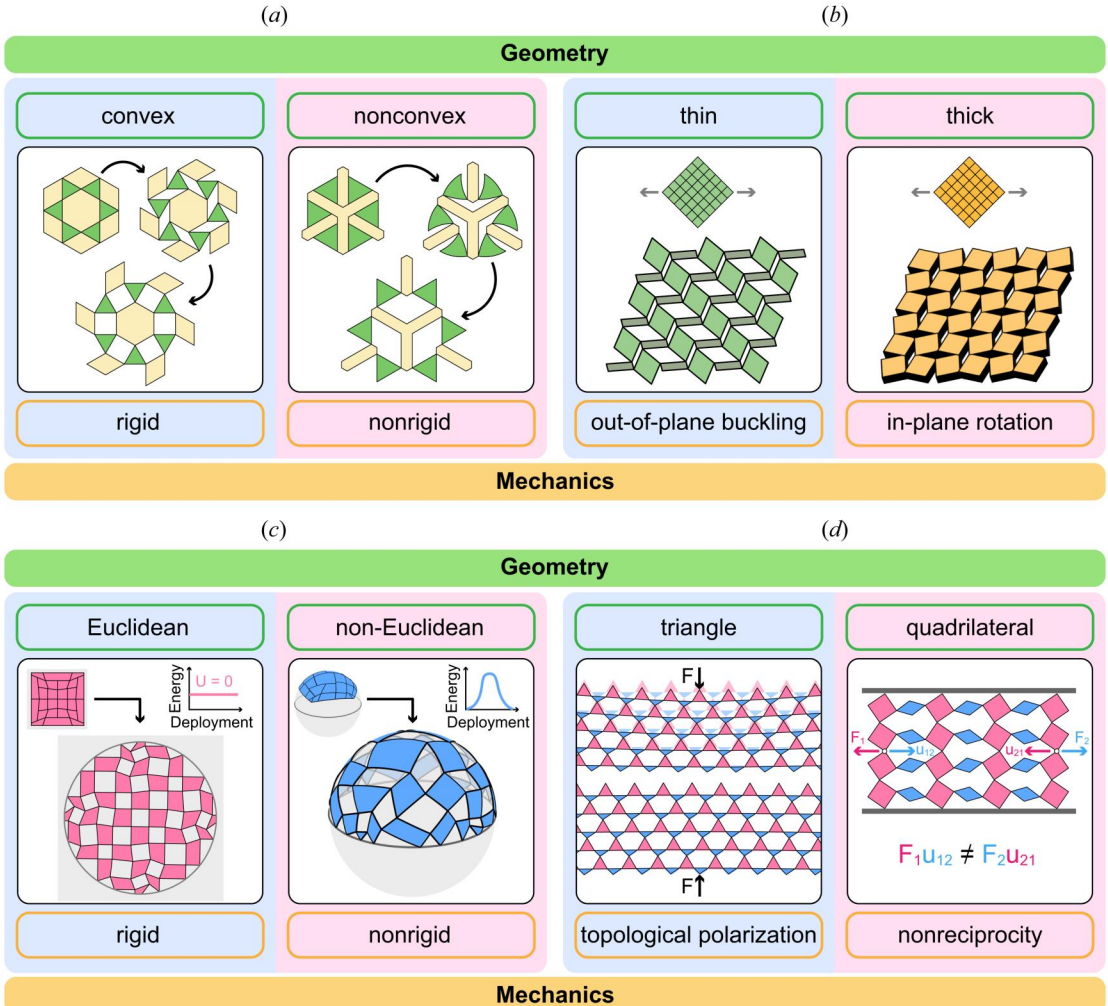


Fig. 1 Kirigami engineering: the interplay between geometry and mechanics: (a) a convex pattern undergoing rigid deformation (left) and a nonconvex pattern undergoing nonrigid deformation (right), (b) a thin rotating-square sheet exhibiting out-of-plane buckling under uniaxial tension (left) and a thick rotating-square plate exhibiting in-plane rotation under uniaxial tension (right), (c) a quadrilateral kirigami pattern in a Euclidean space (the plane) transforming rigidly from a compact square to a deployed circle (left) and a quadrilateral kirigami pattern in a non-Euclidean space (the sphere) displaying nonrigid shape morphing from a compact spherical square to a deployed hemisphere (right), and (d) a triangular kirigami pattern exhibiting topological polarization (left) and a quadrilateral kirigami pattern displaying mechanical nonreciprocity (right)

while practically, the substantial hinge stiffness may hinder the realization of rigid deformation.

2.1 Nonconvexity and Bistability. A bistable structure is nonrigid with an energy barrier on its deformation path. Figure 2(a) illustrates a basic quadrilateral kirigami unit that opens a nonconvex hole during its early stage of expansion [4]. As the structure expands, stresses accumulate until the hole reaches a critical configuration, in which two of its edges become collinear. At this juncture, the deformed lengths are minimal, corresponding to the peak of an energy bump. Once this critical state is surpassed, the stresses drop to zero, and the edges revert to their original lengths. Thereafter, the hole remains convex, and the deformation energy stays at zero. The energy landscape depicted in Fig. 2(a) is computed using a simplified mechanical model that employs linear springs along the edges and diagonals of the quadrilaterals that can undergo both extension and compression. This model is a specific case of a more general framework [5], which incorporates both linear springs and torsional springs located at the nodal hinges connecting the quadrilaterals. In the general formulation, the total (dimensionless)

deformation energy of a quadrilateral kirigami pattern is expressed as

$$E(\mathbf{x}_1, \mathbf{x}_2, \dots, \mathbf{x}_N) = \frac{1}{N_s} \sum_{i,j} \left(\frac{\|\mathbf{x}_i - \mathbf{x}_j\| - \ell_{ij}}{\ell_{ij}} \right)^2 + \frac{\lambda}{N_c} \sum_i \theta_i^2 \quad (1)$$

Here, the nodal coordinates \mathbf{x}_i determine the energy E , by setting the deformed edge lengths $\|\mathbf{x}_i - \mathbf{x}_j\|$ and the opening angles θ_i of the cuts. The geometry of the undeformed kirigami pattern defines the rest lengths ℓ_{ij} of the linear springs, and it is assumed that all cuts are initially closed so that the rest angles of the torsional springs are zero. The displacement energy is averaged over the total number of linear springs N_s and the rotation energy is averaged over the total number of torsional springs N_c . A key coefficient, λ , adjusts the ratio between the rotation energy and the displacement energy. The deformed nodal positions \mathbf{x}_i and the corresponding energy E are obtained by iteratively moving selected control nodes (i.e., a subset of $\{\mathbf{x}_i\}$) toward target positions and minimizing E . In the idealized case where the hinges have zero rotational stiffness ($\lambda = 0$), the deformation energy of the quadrilateral kirigami arises solely from

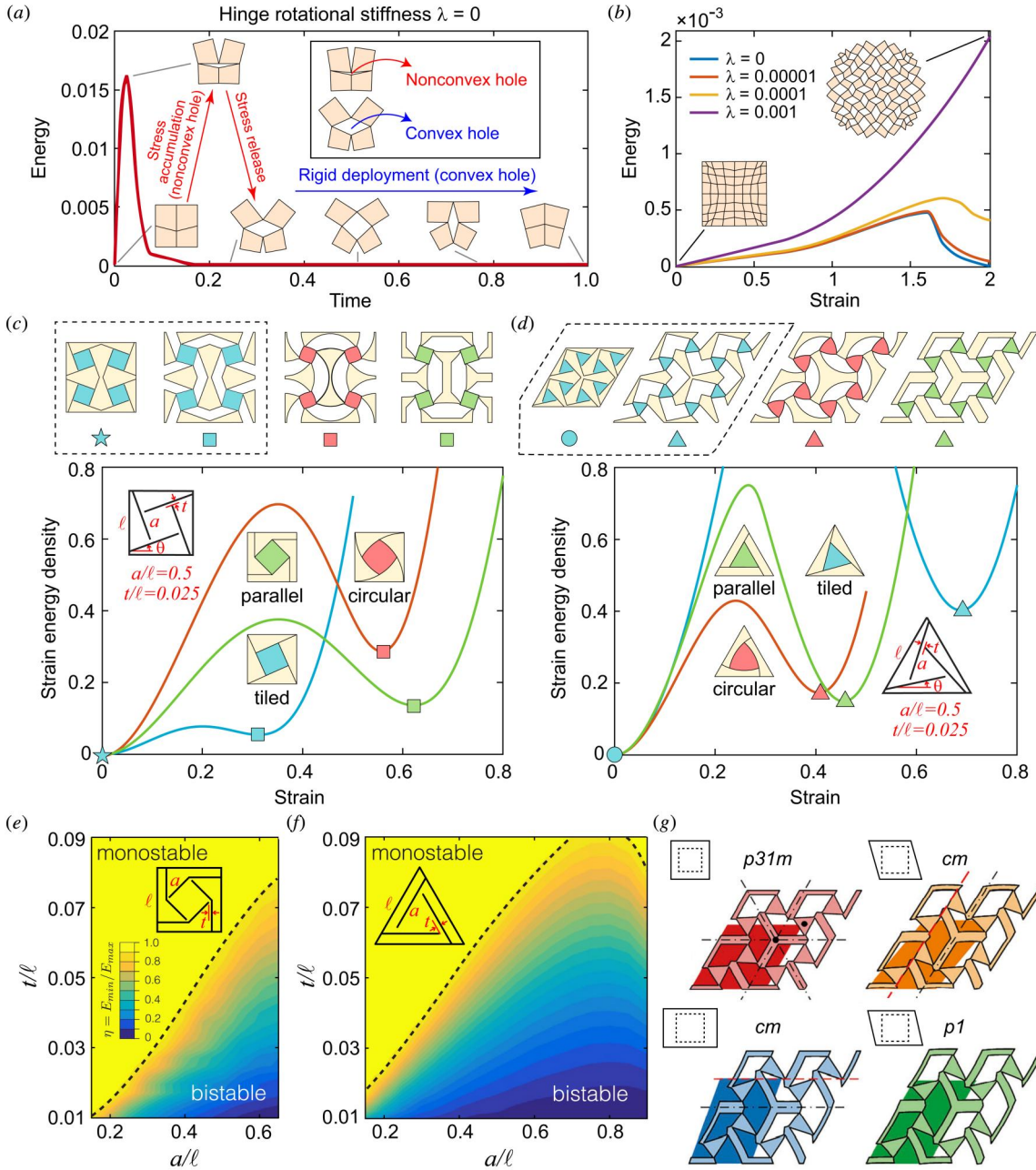


Fig. 2 Nonconvexity-induced bistability of kirigami structures. (a) Energy landscape of a kirigami unit with a nonconvex hole [4]. (b) Energy landscapes of a shape-morphing kirigami tessellation with multiple nonconvex holes under varying rotational stiffness λ [5]. The data and deformation profiles in (a) and (b) are from bar-and-hinge model simulations. (c) and (d) Energy landscapes of motif-inspired kirigami patterns with nonconvex cuts [6]. The patterns in (c) have square cores, while the patterns in (d) have triangular cores. (e) and (f) Phase diagrams showing the ratio of local minimum energy (at the deployed stable state) to the peak energy (corresponding to the energy barrier), $\eta = E_{\min}/E_{\max}$, with respect to the scaled hinge thickness t/ℓ and the scaled unit length a/ℓ of the kirigami units [6]. The unit cell in (e) has a square core, while the unit cell in (f) has a triangular core. When $\eta = 1$, the unit cells are monostable. When $\eta < 1$, the unit cells are bistable. (g) Isotropic (with $p31m$ symmetry) and anisotropic (with cm or $p1$ symmetry) bistable deformations of generalized motif-inspired kirigami patterns [7]. Dashed-dotted lines: reflection axes; dashed lines: glide reflection axes; dots: rotation centers. The data and deformation profiles in (c)–(g) are from finite element simulations. Panel (a) is adapted with permission from Ref. [4]. Copyright 2021 by CC BY 4.0 license. Panel (b) is adapted with permission from Ref. [5]. Copyright 2019 by Springer Nature. Panels (c)–(f) are adapted with permission from Ref. [6]. Copyright 2016 by Elsevier. Panel (g) is adapted from Ref. [7]. Copyright 2024 by CC BY-NC 4.0 license.

the extension or compression of the edges and diagonals, thereby enabling the convex hole to deploy (theoretically) with zero energy cost (Fig. 2(a)).

If a kirigami pattern comprises multiple nonconvex cuts, their collective deployment may yield one or more energy barriers. In

particular, when a single energy barrier is present, the structure is bistable upon deployment. Figure 2(b) illustrates such a bistable pattern (when $\lambda = 0$), achieved by inversely optimizing the cut distributions within a constrained framework [5]. This approach ensures that the deployed boundary nodes align with a target curve

while satisfying the geometric conditions required for closing all the cuts in an undeployed (compact) state. Consequently, the corresponding quadrilaterals in both the undeployed and deployed configurations have identical sizes and shapes. Moreover, by controlling the boundary angles, the shape of the compact pattern can be finely tailored, enabling a smooth transition from a compact square to a deployed circle. It should be noted that the bistability converts to monostability as λ increases, which prevents the cuts from opening (e.g., $\lambda = 0.001$ in Fig. 2(b)). The monostability corresponds to physical prototypes manufactured by laser cutting a rubber sheet and leaving relatively thick ligaments at the intersection of cuts (called *living hinges* or *compliant hinges*) to connect the quadrilateral panels [5]. In contrast, thin ligaments (e.g., $\lambda = 0.0001$ or 0.00001 in Fig. 2(b)) do not significantly impede bistability but are more prone to breakage when the prototype is deployed. The free-form quadrilateral patterns offer an expansive design space for distributing cuts to achieve shape-morphing functionality. However, these patterns are not intentionally designed to be bistable or monostable. The primary goal here is to achieve target shapes instead of tailoring energy landscapes. Although the energy envelopes have a single peak when λ is small, it is challenging to realize this bistability in solid models with living hinges.

Substantial bistability of a class of periodic kirigami patterns with nonconvex cuts is verified through finite element simulations and mechanical tests on perforated rubber sheets—a favorable ligament thickness can sufficiently trigger bistability and resist fracture upon deployment [6]. Here we review only the simulation results and refer to Ref. [6] for the tests on real prototypes. Inspired by ancient geometric motifs, one of these patterns features square modules with four oblique lines enclosing a square core (“tiled” cores in Fig. 2(c)). At the specific ratio of ligament thickness to unit length $t/\ell = 0.025$, finite element simulations reveal weak bistability (the lowest curve in Fig. 2(c)). In contrast, variant patterns obtained by curving or rotating the cores (“circular” or “parallel” cores in Fig. 2(c)) exhibit significantly enhanced bistability, as demonstrated by simulation curves with substantial energy barriers (the two higher curves in Fig. 2(c)). The motif-inspired patterns also include a version with triangular cores (“tiled” cores in Fig. 2(d)) and corresponding variants produced by curving or rotating the cores (“circular” or “parallel” cores in Fig. 2(d)). Interestingly, the original triangular cores exhibit a much higher energy barrier than their variants at $t/\ell = 0.025$, which is the opposite of the behavior observed with the square cores. Furthermore, Figs. 2(e) and 2(f) show that bistability can be achieved within a finite region of ligament thickness for both the square and the triangular “parallel” cores. Specifically, bistability is strong for large a/ℓ and small t/ℓ , because the cuts penetrate deeper into nonconvex shapes as a/ℓ increases and the rotational stiffness of the ligaments becomes smaller as t/ℓ decreases. The triangular patterns with “parallel” cores possess $p31m$ symmetry (with threefold rotations and some rotation centers off mirrors) and exhibit isotropic dilation upon deployment (Fig. 2(g)). In more advanced developments, these triangular patterns are generalized to produce various anisotropic bistable deformations under reduced symmetry—e.g., cm symmetry (with mirrors and glides but no rotation center) and pl symmetry (with no mirror, glide, or rotation center) in Fig. 2(g)) [7]—and even aperiodic bistable deformations [8]. The local nonconvexity of the cuts manipulates the nonrigid deformations of these kirigami patterns. When the patterns are periodic (e.g., those in Figs. 2(c) and 2(d)), their overall behavior mirrors that of the individual unit modules. In contrast, for a free-form pattern (e.g., that in Fig. 2(b)), the interactions among the nonconvex cuts influence the overall energy landscapes, although the rationale behind the presence of only one energy peak is unclear. In fact, the optimization approach (that designs the pattern in Fig. 2(b)) can be generalized to further enable two distinct compact configurations, corresponding to two reverse ways of closing the quadrilateral holes, in the quadrilateral kirigami pattern with multiple nonconvex cuts [4]. Under this extended framework, the designed kirigami pattern exhibits two energy barriers near the compact states, connected by an intervening

mechanism. A systematic method for designing the number and location of the energy barriers (or energy minima) has yet to be fully developed.

2.2 Compatibility and Rigid Deformation. It is noteworthy that nonconvexity is neither a sufficient nor a necessary condition for nonrigid deformations in a kirigami pattern. Nonrigid deformations arise when the deployment of a nonconvex cut forces the panel edges to deform due to the geometric confinement (Fig. 1(a), right, and Fig. 2(a)). In the absence of such confinement, even nonconvex cuts (e.g., in rotating triangles [9]) can support rigid deformations. Conversely, although a single convex cut is generally rigidly deployable—yielding rigidly deployable periodic patterns (e.g., rotating squares [10])—the overall deformation of free-form patterns with multiple convex cuts can be either rigid or nonrigid, depending on the interactions among the cuts. Such interactions are quantified by a *compatibility condition* (or termed *loop condition*) for a class of free-form patterns named *planar quadrilateral kirigami (PQK)* [11]. While the PQK is composed of arrayed quadrilateral panels and cuts, it is free-form in the sense that the panels and cuts can be arbitrary quadrilaterals as long as the cuts are convex, i.e., they can close to a straight line.

Figure 3(a) shows a 3-by-3 PQK pattern with four interconnected cuts forming a loop. Each cut is a convex quadrilateral, satisfying $a_i + b_i = c_i + d_i$ for $i = 1, 2, 3, 4$, so that they can individually deploy with one degree-of-freedom, characterized by an opening angle α_i or β_i (i can be 1, 2, 3, or 4). To obtain the loop condition, we suppose that the collective deployment of the four cuts is rigid. Then, the connections between the cuts imply that the opening angle of one cut, e.g., β_1 , determines the opening angles of its neighboring cut, e.g., α_4 and β_4 , expressed by

$$\alpha_i = \pi - \beta_{i+1} \quad (2)$$

and

$$\cos \beta_i = g_i(\cos \beta_{i+1}) \quad (3)$$

respectively, where the index i cycles from 1 to 4 (with $i + 1$ taken as 1 when $i = 4$). The function g_i maps the opening angle β_{i+1} in one cut to its counterpart β_i in the adjacent cut. The form of g_i depends on the cut side lengths a_i, b_i, c_i, d_i and is given explicitly by [11]

$$g_i(x) = \cos \left(\arccos \frac{a_i^2 + e_i^2 - d_i^2}{2a_i e_i} + \arccos \frac{b_i^2 + e_i^2 - c_i^2}{2b_i e_i} \right) \quad (4)$$

with

$$e_i = \sqrt{a_i^2 + d_i^2 + 2a_i d_i x} \quad (5)$$

The loop formed by the four cuts naturally leads to the composition

$$g \triangleq g_1 \circ g_2 \circ g_3 \circ g_4 \quad (6)$$

which maps β_1 to a new angle $\hat{\beta}_1$ such that $\cos \hat{\beta}_1 = g(\cos \beta_1)$. The operator \circ refers to the function composition, e.g., $(g_1 \circ g_2)(x) = g_1[g_2(x)]$. This process is shown in Fig. 3(a). For a deployed configuration where the panels remain undeformed and the connections intact, β_1 must be invariant under the map g . This requirement defines the compatibility condition

$$g(\cos \beta_1) = \cos \beta_1 \quad (7)$$

When all the cuts are parallelograms (i.e., $a_i = c_i$ and $b_i = d_i$, $i = 1, 2, 3, 4$), g reduces to an identity function $g(x) = x$, so the compatibility condition (7) holds for any $\beta_1 \in [0, \pi]$, as indicated by the straight line in Fig. 3(c). In this case, the 3-by-3 PQK is rigidly deployable.

As long as all the cuts are parallelograms, general M -by- N PQK is also rigidly deployable, because the compatibility condition can be

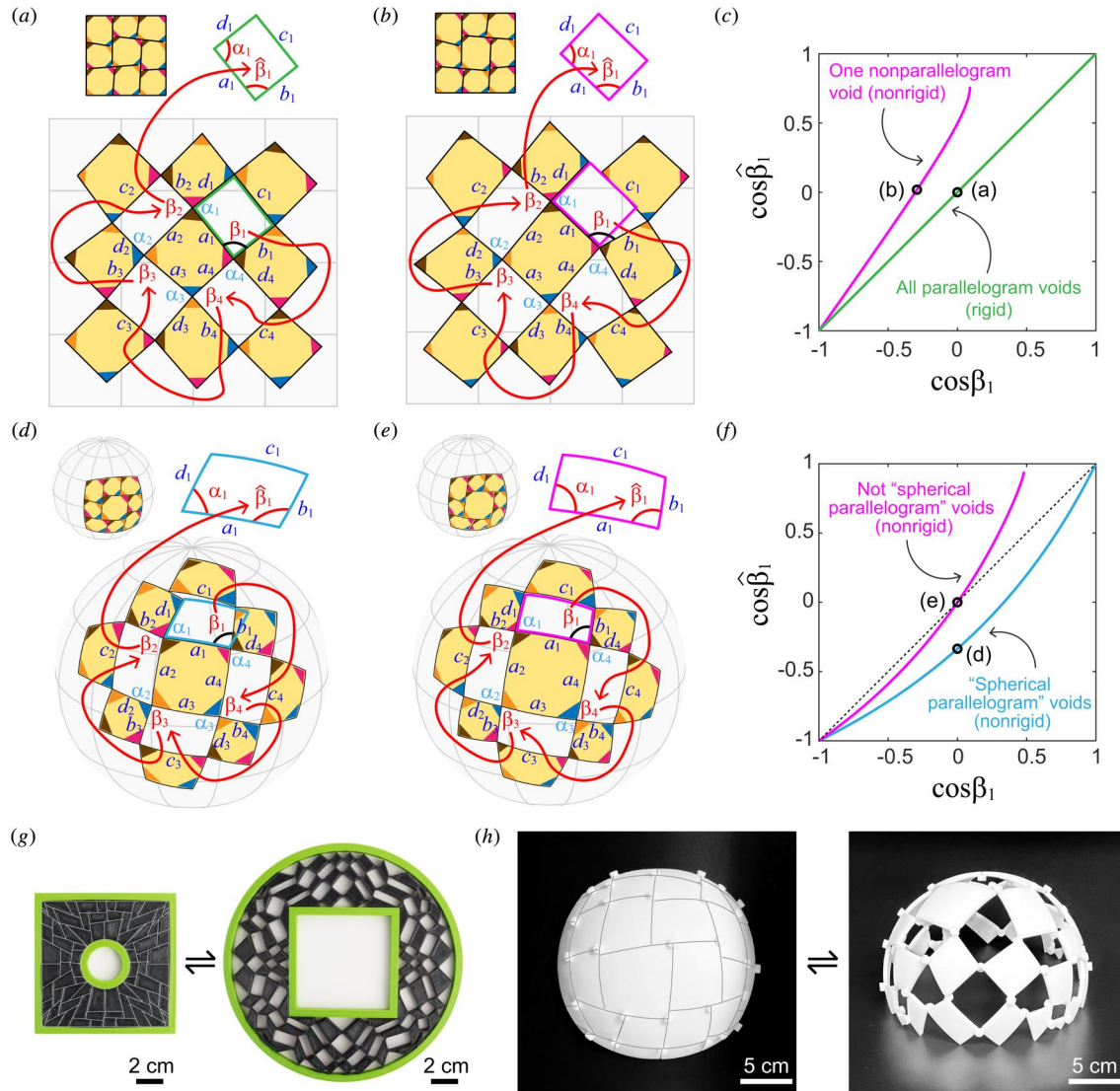


Fig. 3 Compatibility-induced rigidly deployable kirigami versus incompatible-induced nonrigidly deployable kirigami. (a) and (b) Deployment of 3-by-3 planar quadrilateral kirigami pattern. Notice that, in (a), all the four voids are parallelograms while, in (b), only three voids are parallelograms (the void at the bottom-right is not a parallelogram). (c) The curves of $\cos \beta_1$ versus $\cos \beta_1$ for the planar kirigami patterns. (d) and (e) Deployment of 3-by-3 spherical quadrilateral kirigami [13]. All the four cuts in (d) are spherical parallelograms, while those in (e) are not spherical parallelograms. (f) The curves of $\cos \beta_1$ versus $\cos \beta_1$ for the spherical kirigami in (d) and (e) [13]. In (a), (b), and (d), (e), the opening angles α_i , β_i , γ_i , δ_i ($i=1, 2, 3, 4$) and β_1 can be determined by the geometry of these patterns (i.e., the side lengths a_i , b_i , c_i , and d_i , for $i=1, 2, 3, 4$) and one opening angle, say, β_1 . The arrows show the dependence of these angles from β_1 to β_1 . (g) A genus-1 planar kirigami prototype that can morph between a compact state with a circular hole inside a square (left) and a deployed state with a square hole inside a circle (right). The prototype was 3D-printed using thermoplastic polyurethane (TPU). The frames were 3D-printed using polylactic acid (PLA). (h) A spherical kirigami prototype that can morph between two stable states—a compact spherical square and a deployed dome [13]. The prototype was assembled by joining 3D-printed resin panels at their pin joints. In (g) and (h), auxiliary gray lines highlight the cut distributions on the compact configurations. Panels (d), (e), (h) are adapted with permission from Ref. [13], Copyright 2022 by American Physical Society.

verified for any loop of cuts. A rigidly deployable PQK pattern can be generated by solving a system of linear equations based on given coordinates of a subset of nodes and given cut aspect ratios. This procedure can be implemented either through a global construction [11] or an additive construction [12]. In both cases, the linear nature of rigidly deployable PQK streamlines the inverse design process. Figure 1(c), left, illustrates a shape-morphing kirigami pattern obtained by the global approach [11]. The kirigami pattern is formed by parallelogram cuts, which determines the rigid deployment from a square to a circle. Moreover, the aforementioned PQK can be further generalized to genus- n PQK—characterized by n holes in its global geometry—whose rigid deployability is guaranteed by the

existence of a deployed state with parallelogram cuts. Under this terminology, the original PQK is genus-0. It is important to note that the existence of a deployed state essentially imposes an additional constraint to a genus- n PQK pattern. In other words, while genus-0 PQK necessarily possesses a (rigidly) deployed state if all cuts are parallelograms, genus- n ($n \geq 1$) PQK with parallelogram cuts may not have a (rigidly) deployed state [11].

The generalization to genus- n paves the way for more sophisticated inverse designs, such as tailoring both the exterior and interior boundary shapes. Figure 3(g) shows a genus-1 PQK prototype. In the compact state, the exterior boundary forms a square, while the interior boundary approximates a circle. By

deploying the prototype, these shapes can be reversed: the exterior boundary becomes circular, and the interior boundary becomes square. The prototype was 3D printed using thermoplastic polyurethane (TPU). Although the PQK is rigidly deployable in theory—since its voids (i.e., small holes) are all parallelograms and a deployed state exists—stresses accumulate at the living hinges during deformation. As a result, the prototype is monostable. Stiff frames (made of polylactic acid, PLA) are used to lock the deformation.

It is noteworthy that the shape-morphing kirigami shown either in Figs. 2(b) or 3(g) is designed through numerical optimization. Leveraging local deformation characteristics of the rotating units, the inverse design may be alternatively achieved in a “numeric-free” manner. This principle has been applied to triangular patterns, where the design is implemented by directly transforming the nodal coordinates of a standard kagome pattern, guided by the maximum shear strain distribution associated with the target shape change [9].

2.3 Incompatibility and Nonrigid Deformation. We have shown that the existence of a deployed state with parallelogram cuts is sufficient for the rigid deployability of PQK. But is this condition also necessary? The answer is yes. In fact, even if only one cut is not a parallelogram, it can be proven that $g'' > 0$ under the constraint $a_i + b_i = c_i + d_i$, $i = 1, 2, 3, 4$ [11]. This implies that g is a strict convex function. Consequently, the compatibility condition (7) can be satisfied for at most two distinct values of β_1 , and therefore the PQK is not rigidly deployable. As illustrated in Fig. 3(b), nonrigid 3-by-3 PQK must break a hinge connection to preserve the sizes and shapes of panels when β_1 violates the compatibility condition (since $\tilde{\beta}_1 \neq \beta_1$). This behavior is depicted by the higher curve in Fig. 3(c). If general M -by- N genus- n PQK has at least one nonparallelogram cut, it is not rigidly deployable, since every 3-by-3 section containing that cut loses rigid deployability. Our discussion indicates that the rigid (or nonrigid) deformations of PQK are fundamentally determined by the geometric compatibility (or incompatibility) of its constituent cuts. This insight is captured in the following theorem [11]:

THEOREM 1 (genus- n deployability). *Genus- n ($n \geq 0$) PQK is rigidly deployable if and only if there exists a deployed state with all the cuts forming parallelogram voids.*

THEOREM 1 indicates that it is possible to customize rigid or nonrigid deformations of free-form quadrilateral kirigami on a plane. This diversity of deformation features is essentially facilitated by the planarity of the space where the PQK reside. In contrast, if the space is intrinsically curved, i.e., of nonzero Gaussian curvature, achieving rigid deployment may be impossible for a loop of cuts. A study on this issue is conducted for *spherical quadrilateral kirigami* (SQK), which retains the same nodal connections as PQK, but all the straight cuts on a plane become geodesic lines (i.e., great-circle arcs) on a sphere [13]. Figure 3(d) shows a 3-by-3 SQK pattern that is an analogy to the rigidly deployable PQK with parallelogram cuts. That is, opposite side lengths are equal for each cut, expressed by $a_i = c_i$ and $b_i = d_i$ for $i = 1, 2, 3, 4$. Here, the side lengths a_i , b_i , c_i , and d_i are geodesic lengths on the sphere. For conciseness, we call the cuts with equal opposite side lengths *spherical parallelogram* cuts. We suppose that the Gaussian curvature of the base sphere is K . The compatibility condition still has the form (7), while the loop function g becomes [13]

$$g^e(x) = \frac{(P+Q)x + (P-Q)}{(P+Q) + (P-Q)x} \quad (8)$$

with

$$P, Q = \prod_{i=1}^4 \cos^2 \left[\frac{(a_i \pm b_i)\sqrt{K}}{2} \right] \quad (9)$$

In this case, the compatibility condition (7) has two solutions $\cos \beta_1 = \pm 1$, indicating that the 3-by-3 SQK only has two

compatible configurations. These two configurations are both compact, with all the cuts closed, as captured by the lower curve in Fig. 3(f). For M -by- N SQK with spherical parallelogram cuts, the compatible configurations are also two compact configurations as consistent with all its 3-by-3 parts. In other words, the SQK with spherical parallelogram cuts is not rigidly deployable, which is essentially different from the rigidly deployable PQK with parallelogram cuts. This difference in deployability originates from different Gaussian curvatures between the sphere and the plane. With a simplified spring model, the nondimensionalized deployment energy \tilde{E}_S of the 3-by-3 SQK with parallelogram cuts can be expressed by [13]

$$\tilde{E}_S = \frac{1}{8} \left[\sum_{i=1}^4 (a_i b_i) \right]^2 K^2 \sin^4 \beta_1 + O[L^6 K^3] \quad (10)$$

where $L = \max\{a_1, b_1, \dots, a_4, b_4\}$. Equation (10) clearly shows that zero K leads to zero \tilde{E}_S , suggesting the rigid deployability for PQK. By contrast, \tilde{E}_S is positive for nonzero K at $\cos \beta_1 \in (-1, 1)$, indicating the nonrigid deployability for SQK. When $\cos \beta_1 = \pm 1$, \tilde{E}_S is zero even for nonzero K , corresponding to the two compact compatible configurations. By perturbing the nodal positions of the SQK patterns with spherical parallelogram cuts (e.g., the one in Fig. 3(d)), the compatible configuration at $\cos \beta_1 = 1$ can be moved to inside $(-1, 1)$, e.g., at $\cos \beta_1 = 0$ as shown in Fig. 3(e) and by the higher curve in Fig. 3(f). After the perturbation, the cuts are not necessarily spherical parallelograms, but the cut side lengths a_i, b_i, c_i, d_i still satisfy $a_i + b_i = c_i + d_i$ for $i = 1, 2, 3, 4$, guaranteeing that the cuts can close to geodesic lines at $\cos \beta_1 = -1$. Under this condition, it can be proven that $g'' > 0$ for $\cos \beta_1 \in [-1, 1]$, so that the loop function g (whose special form is g^e when $a_i = c_i$ and $b_i = d_i$) is a strict convex function and the compatibility condition (7) holds true only for at most two distinct values of β_1 [13]. This means 3-by-3 SQK, with either spherical parallelogram or nonparallelogram cuts, is not rigidly deployable, and consequently, general M -by- N SQK is not rigidly deployable because it contains 3-by-3 components. This conclusion is described by the following theorem [13]:

THEOREM 2 (Spherical compatibility). *SQK has either one or two compatible configurations.*

Figures 3(d)–3(f) illustrate the SQK patterns with two compatible configurations. Certain SQK patterns may also have only one compatible configuration, i.e., the undeployed configuration. We refer to the supplementary material of Ref. [13] for such cases. Theorems 1 and 2 reveal that the Gaussian curvature plays a critical role for the deployment of kirigami structures. While on a plane, one can design a rigidly deployable kirigami pattern whose boundary morphs from a square to a circle (Fig. 1(c), left), such morphing pattern is bistable on the curved sphere (Fig. 1(c), right). Figure 3(h) shows a prototype that can be deployed from a compact spherical square to a compatible dome with its boundary forming a small circle. The square and the dome have the same radius of curvature. The resin panels were 3D printed separately and then assembled at the pin joints. The pin joints can rotate freely so the prototype is bistable as predicted by the compatibility theorem.

Kirigami deployment on a general curved surface is an intriguing topic that deserves further studies. However, rigid kirigami panels with fixed curvatures cannot be freely deployed/moved within a surface with varying curvatures. Instead, the kirigami panels need to be flexible/soft in order to deform and to fit a curved surface with an inhomogeneous curvature distribution [14]. The compatibility on a generally curved surface may be defined by an optimization framework and may be material-dependent.

2.4 Symmetry Considerations. Many classical kirigami patterns are periodic tessellations such as the kagome kirigami (Fig. 4(a)) and the rotating-square kirigami (Fig. 4(b)). These tessellations can be characterized by the *wallpaper groups* (or termed *plane crystallographic groups*), which contain two

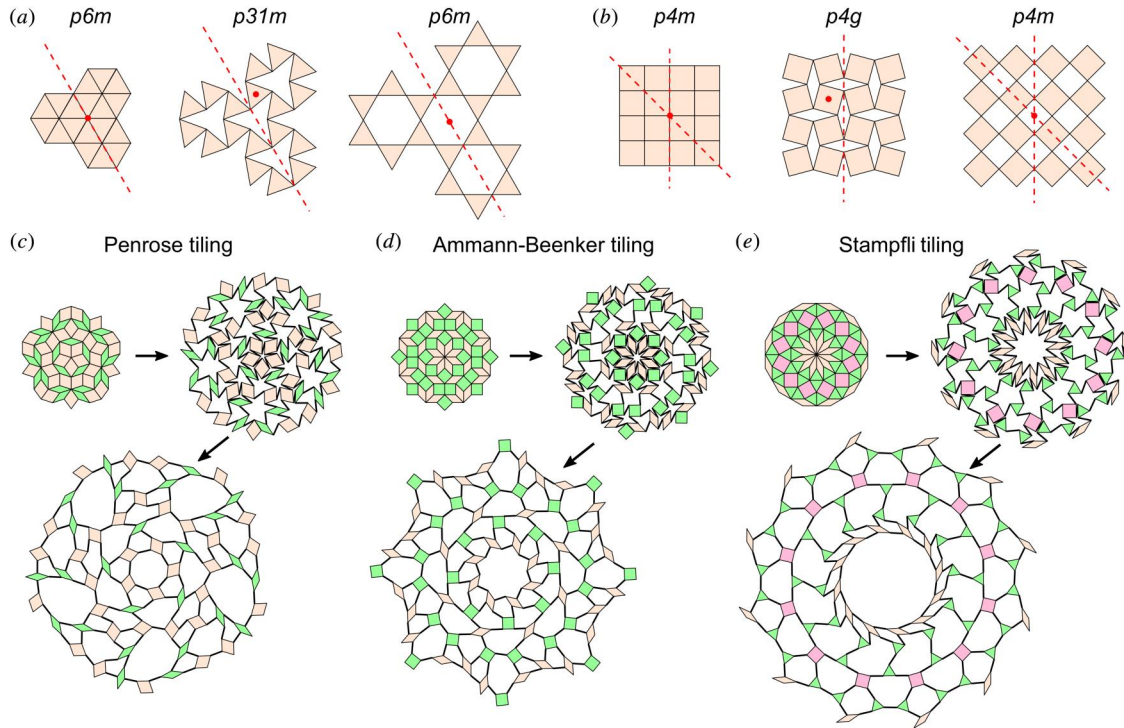


Fig. 4 Plane symmetry group and quasi-crystal kirigami. (a) and (b) Wallpaper group kirigami [16]. (a) The kagome kirigami pattern has $p6m$ symmetry (a six-fold rotation center plus reflection axes) at the compact (left) and fully deployed (right) states while the partially deployed configuration (middle) has $p31m$ symmetry (an off-mirror three-fold rotation center plus reflection axes). (b) The rotating-square kirigami pattern has $p4m$ symmetry (a four-fold rotation center plus reflection axes at 45 deg) at the compact (left) and fully deployed (right) states while the partially deployed configuration (middle) has $p4g$ symmetry (a four-fold rotation center plus reflection axes at 90 deg). In (a) and (b), key rotation centers (dots) and reflection axes (dashed lines) that can be used for determining their wallpaper group types are highlighted. (c)–(e) Quasi-crystal kirigami [17]. (c) A fivefold Penrose kirigami pattern. (d) An eightfold Ammann–Beenker kirigami pattern. (e) A twelvefold Stampfli kirigami pattern. In (c)–(e), the compact states, intermediate deployed states, and the fully deployed states are shown. Panels (a) and (b) are reproduced with permission from Ref. [16], Copyright 2021, the Author(s). Panels (c)–(e) are reproduced from Ref. [17], Copyright 2022 by CC BY 4.0 license.

independent translators [15]. There are in total seventeen wallpaper groups representing all the planar translational symmetries distinguished by rotation, reflection, and glide reflection (see Table 1). The kagome pattern is $p6m$, featuring sixfold rotations and reflections in six distinct directions. The rotating-square pattern is $p4m$, featuring fourfold rotations and reflections in four distinct directions. Both the kagome pattern and the rotating-square pattern are rigidly deployable. Wallpaper groups can also describe some bistable patterns. For example, the motif-inspired patterns with square cores (Fig. 2(c), top left) are $p4g$, featuring fourfold rotations and reflections in only two directions; the motif-inspired patterns with triangular cores (Fig. 2(d), top left) are $p31m$, featuring threefold rotations and rotation centers off mirrors. The bistable patterns are not rigidly deployable, but still deployable, i.e., compatible between a compact configuration and a frustration-free expanded configuration. In fact, for any of the seventeen wallpaper groups, one can construct deployable kirigami with the corresponding symmetry. The symmetry can be specified for either the compact or the deployed pattern. This insight is established in the following two theorems [16]:

THEOREM 3 (wallpaper group deployability: compact pattern). *For any group G among the 17 wallpaper groups, there exists a deployable kirigami pattern in G .*

THEOREM 4 (wallpaper group deployability: deployed pattern). *For any group G among the 17 wallpaper groups, there exists a deployable kirigami pattern with its final deployed shape in G .*

These two theorems are proven by explicitly presenting the kirigami patterns for all seventeen wallpaper groups [16]. Moreover,

one can build connections between compact and deployed symmetric patterns with arbitrary size change or symmetry change. This conclusion is established in the following two theorems [16]:

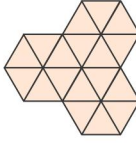
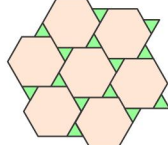
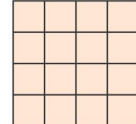
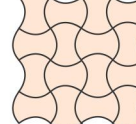
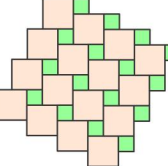
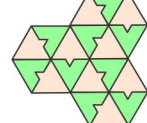
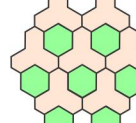
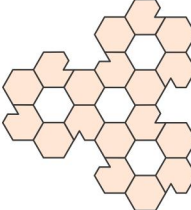
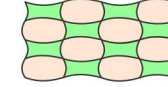
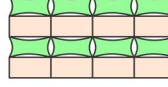
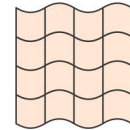
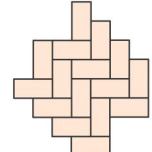
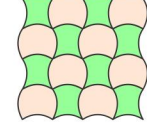
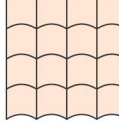
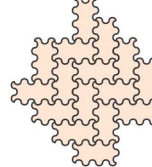
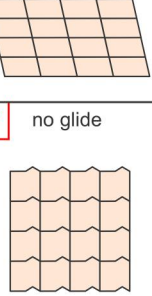
THEOREM 5 (Wallpaper group deployability: Size change). *For any deployable wallpaper group pattern with n -fold rotational symmetry, we can design an associated pattern with n -fold rotational symmetry and arbitrary size change.*

THEOREM 6 (Wallpaper group deployability: Symmetry change). *Gain, loss and preservation of symmetry are all possible throughout the deployment of a kirigami pattern.*

The arbitrary size changes can be achieved through symmetry-preserving expansion to cuts or panels. The arbitrary symmetry changes are justified with specific kirigami patterns, for example, the temporal rotational symmetry loss ($p6m$ to $p31m$ to $p6m$) in Fig. 4(a) and the reflectional symmetry preservation ($p4m$ to $p4g$ to $p4m$) in Fig. 4(b).

The wallpaper groups can describe rotational symmetries of order 1, 2, 3, 4, or 6. *Quasi-crystal kirigami* expands the design space of deployable kirigami beyond the wallpaper groups to quasi-crystal tilings, which lack translational symmetry but can exhibit high-order rotational symmetries such as fivefold (Penrose tiling), eightfold (Ammann–Beenker tiling), and twelvefold (Stampfli tiling) [17]. Starting from given compact quasi-crystal tilings, rigidly deployable kirigami patterns can be obtained by adding tiles (the expansion tile method), removing tiles (the tile removal method), or changing the connectivity of the tiles (the Hamiltonian cycle method). The expansion tile method achieves significant size change upon deployment of the kirigami (Figs. 4(c)–4(e)). The tile removal

Table 1 Characterization of the 17 wallpaper groups and the kirigami patterns [15,16]

rotational symmetry	has reflectional symmetry			no reflectional symmetry
6-fold	<p>p6m</p> 			p6 
4-fold	p4m mirrors at 45° 	p4g mirrors at 90° 	p4 	
3-fold	p31m some rotation centers off mirrors 	p3m1 all rotation centers on mirrors 	p3 	
2-fold	cmm orthogonal mirrors & some rotation centers off mirrors 	pmm orthogonal mirrors & all rotation centers on mirrors 	pmg only parallel mirrors 	pgg has glides 
1-fold (none)	cm has glides 	pm no glide 	pg has glides 	p1 no glide 

Images are adapted or reproduced with permission from Ref. [16], Copyright 2021 by the Author(s).

method reduces the overall size change accompanied by the variation of void shapes. The Hamiltonian cycle method can realize extremely large size change throughout the kirigami deployment.

3 On Three-Dimensional Deformations

From a physical perspective, two key factors govern the deformation of kirigami surfaces with living hinges. The first factor is the distribution of cuts. By assuming in-plane (or generally, in-surface) rotations, one can analyze the 2D deformation characteristics based solely on the cut distribution. Such analysis is reviewed in Sec. 2 to characterize stability (Fig. 2), rigid or nonrigid deformation (Fig. 3), and deformation symmetry (Fig. 4). While the in-plane stiffness of the living hinges may affect the deformation energy landscapes (e.g., transferring a theoretically bistable pattern into monostable as shown in Figs. 2(e) and 2(f)), it has little effect on the deformed shape as predicted in theory, as long as the deformation is within the 2D surface (e.g., Fig. 3(g)). By contrast, a more intrinsic geometric parameter—which is the second factor governing the deformation of kirigami surfaces with living hinges—is the ratio of the sheet thickness to the ligament width. This factor controls the

emergence of out-of-plane deformation of a flat sheet. In addition, the kirigami hinges can be intentionally endowed with rotational axes biased from the normal of the kirigami surface. This implementation facilitates 3D shape morphing under controllable deformations.

3.1 Buckling of Thin Kirigami Sheets. Figure 5(a) illustrates a rotating-square plastic sheet that is stretched in the direction along the square diagonals. The geometry of the sheet is described by its thickness t , ligament width δ , and square length ℓ . The in-plane bending of the ligaments occurs at the initial deformation stage, with the stiffness of the sheet expressed by [18]

$$\bar{E} = \frac{2}{3} E \left(\frac{\delta}{\ell} \right)^2 \quad (11)$$

in which E is Young's modulus of the material. Once the in-plane strain increases to a critical value ε_c , the ligaments may buckle out-of-plane, causing 3D deformation of the sheet. Assuming that the initial buckling occurs in the small deformation regime, the critical strain ε_c can be derived as [18]

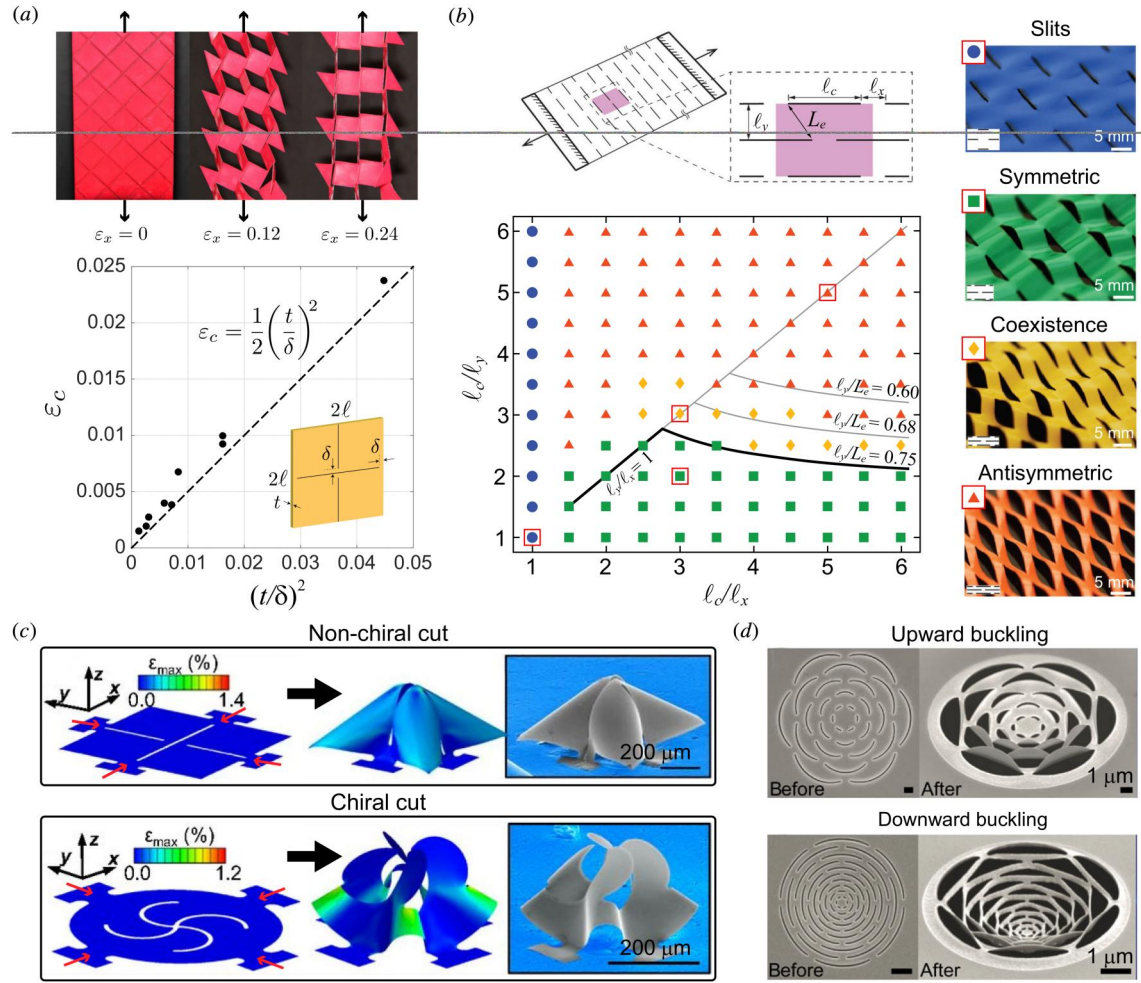


Fig. 5 Out-of-plane buckling in kirigami. (a) A thin kirigami sheet with square cuts (scaled sheet thickness $t/\delta \approx 0.085$ and scaled hinge width $\delta/\ell=0.06$) that buckles under uniaxial tension 45 deg inclined to the cuts (top) and the critical strain ε_c that triggers the buckling of such kirigami sheets as a function of $(t/\delta)^2$ (bottom) [18]. The dots are from experimental data and the dashed line is from theoretical prediction. (b) Parallel cutting sheets [22]. Geometry of the sheets is determined by the cut length ℓ_c , the transverse spacing ℓ_x , and the longitudinal spacing ℓ_y (top left). The phase diagram shows buckling configurations of these sheets under uniaxial tension with respect to the geometric parameters ℓ_c/ℓ_y and ℓ_c/ℓ_x (bottom left). Representative buckled prototypes are provided (right). (c) Nanomembranes (bilayer of silicon nanomembrane and thin polymer film) with cross-cuts (top left) and chiral curve-cuts (bottom left) can transform into 3D buckled configurations (finite element simulations, middle; scanning electron microscopy (SEM) images, right) under compressive loading (arrows at the anchors) [23]. (d) Gold nanofilms with flower-like cuts (top left) and concentric cuts (bottom left) can transform to 3D buckled configurations (right) under global ion beam irradiation (SEM images) [28]. Panel (a) is adapted with permission from Ref. [18], Copyright 2017 by American Physical Society. Panel (b) is adapted with permission from Ref. [22], Copyright 2018 by American Physical Society. Panel (c) is adapted with permission from Ref. [23], Copyright 2015 by the PNAS license. Panel (d) is adapted from Ref. [28], Copyright 2018 by the CC BY-NC 4.0 license.

$$\varepsilon_c \approx \frac{1}{2} \left(\frac{t}{\delta} \right)^2 \quad (12)$$

Equation (12) shows that the critical strain ε_c depends only on the ratio of sheet thickness to ligament width, t/δ . If the sheet is thin enough compared to the ligament width, the buckling happens easily. For example, when $t/\delta \approx 0.085$ (corresponding to the prototype in Fig. 5(a), top), one can calculate $\varepsilon_c \approx 0.0036$. Conversely, a thicker sheet makes it harder for buckling to occur.

Another type of kirigami that exhibits out-of-plane buckling has linear parallel cutting patterns, also known as *ribbon kirigami*, facilitating extremely high stretchability [19–21]. The buckled profile of ribbon kirigami is largely affected by cutting distance [22]. As illustrated in Fig. 5(b), the two parameters ℓ_c/ℓ_x and ℓ_c/ℓ_y dictate the 3D buckling configurations of the thin polyethylene terephthalate (PET) sheets. Here, ℓ_c is the cut length; ℓ_x and ℓ_y are the

spacing between two adjacent cuts in the transverse and longitudinal directions, respectively. First, if the transverse spacing is large (i.e., $\ell_c/\ell_x = 1$), the cuts do not overlap in the longitudinal direction, causing weak interactions and small out-of-plane deformation. Second, if there is overlap between the cuts (i.e., $\ell_c/\ell_x > 1$), large out-of-plane deformations occur, leading to symmetric or antisymmetric buckling configurations. Roughly speaking, when the longitudinal spacing is small (i.e., large ℓ_c/ℓ_y), the buckled sheet is antisymmetric and the configuration is monostable. In contrast, when the longitudinal spacing is large (i.e., small ℓ_c/ℓ_y), the buckled sheet can be symmetric. In this case, each repeating unit is bistable and switchable between the symmetric state and the antisymmetric state under external indentation. The coexistence of symmetric and antisymmetric states can spontaneously appear when the cutting geometry transits from the symmetric side to the antisymmetric side. We refer to Ref. [22] for more rigorous geometric mechanics of the symmetric/antisymmetric state selection, in which the competition

between the bending energy of the plates U_b and the elastic energy of hinges U_h in the symmetric configuration is analyzed. The competition is dominated by the geometry of the cuts, expressed as follows [22]:

$$\frac{U_b}{U_h} \sim \frac{\ell_y \ell_y}{\ell_x L_e} \quad (13)$$

in which $L_e = \sqrt{(\ell_c - \ell_x)^2/4 + \ell_y^2}$ is the effective longitudinal spacing between the cuts. In Fig. 5(b), the symmetric patterns exist approximately in the regime that $\ell_y/\ell_x > 1$ and $0.75 < \ell_y/L_e < 1$, suggesting large U_b over small U_h . In contrast, if U_h is large for the symmetric configuration, the buckled sheet tends to have antisymmetric configuration, in which the elastic hinge has almost no deformation, i.e., U_h is almost zero.

The buckling of thin kirigami sheets can be triggered by compression loading as well. This effect is used in a mechanically driven approach to assemble complex 3D structures from 2D membranes, in scales from macro to micro-and nano-and in materials ranging from monocrystalline silicon to plastic and metal [23]. With the cutting patterns on the membranes, in-plane compressive forces (introduced via prestrained elastomer substrates) can induce out-of-plane buckling, transforming flat precursors into deterministic 3D configurations. The cuts can be designed to define the buckled geometries. For example, as illustrated in Fig. 5(c), the cross-cut pattern (top) generates a pyramidal structure with mirror symmetry while the chiral curve-cut pattern (bottom) assembles a circular configuration with rotational symmetry. Moreover, this mechanical-driven assembling strategy can be applied to hybrid membrane-ribbon systems [23], multi-layered ribbons [24], and hybrid origami-kirigami membranes [25]. All these assemblages demonstrate *out-of-plane popping* with compressive forces applied to the discrete anchors. Similar popping effects arise when chiral kirigami membranes with continuously closed boundaries are subjected to controlled stretching and release [26] or when engineering steel sheets with chiral cuts are directly lifted out-of-plane [27].

In addition to stretching or compression, kirigami buckling can be induced by noncontact loading. For example, the perforated gold nanofilm buckles under global ion beam irradiation [28], as illustrated in Fig. 5(d). The buckling profile is governed by the geometry of the slits. The cantilevers bend upward in the flower-like pattern (Fig. 5(d), top) while the thin strips bend downward in the concentric pattern (Fig. 5(d), bottom).

3.2 Eliminating Out-of-Plane Deformations With Folds and Cuts.

As reviewed above, the out-of-plane buckling can be leveraged to induce desired 3D deformations in thin kirigami sheets. However, the out-of-plane motion is detrimental to the kirigami mechanisms that perform their functionality only inside a plane [4,12,29]. Fabricating kirigami mechanisms aimed at in-plane deformations primarily involves 3D printing [29], cutting thick plates [5], molding [12], or assembling building blocks [4]. The first three approaches commonly use tough materials (e.g., TPU for 3D printing, rubber for cutting, liquid rubber, or plastic for casting) to create the ligaments that serve as compliant hinges. It is crucial to balance the stiffness and strength of the compliant hinges: a large ligament enhances strength and prevents failure, but it also increases rotational stiffness, inducing considerable restoring forces that impede the opening/closing of cuts. One promising way to soften the hinges while not trading off their strength is to introduce fabric hinges that weave through the rubber or plastic panels during the molding process [12,30]. The assembling approach involves fabricating each panel separately (e.g., through 3D printing or folding paper) and connecting the panels with tape [4]. The fabrics or tape, as living hinges, provide very low rotational stiffness, beneficial for free in-plane rotation. However, they may suffer from low out-of-plane stiffness. As a result, the kirigami mechanisms with such hinges may be too flexible to maintain their planar shape without external support.

If out-of-plane buckling is undesired for thin kirigami sheets, the most straightforward solution is to constrain the sheets in a plane. However, this may cause large in-plane bending stress at the ligaments. For example, the cutting end easily breaks when a rotating-square paper unit is stretched (Fig. 6(a), inset). The stress concentration can be eliminated by introducing additional folds into the cuts. Figure 6(a) illustrates the kagome kirigami (left) and the rotating-square kirigami (right) deployed with designed mini folds [31]. At each cutting end, three folds are added to make a protruding tetrahedron hinge, which offers one degree-of-freedom of rotation for the in-plane deformation of the kirigami. This kinematics is consistent with that of the ideal rotating-square kirigami in which axial rotation at the cutting ends drives the opening and closing of cuts. There is no tendency of buckling for the in-plane deformation of the kirigami sheets with folding hinges, which are therefore kirigami mechanisms. Moreover, the folding hinge can have one more degree-of-freedom if out-of-plane deformation is allowed. The multiple degrees-of-freedom can be harnessed to produce multimodal deformations of the kirigami sheets [31].

By combining cutting, folding, and pasting, one can introduce intrinsic curvature to a flat surface and transform it into complex 3D structures of finite thickness. This principle underlies the concept of *lattice kirigami*, in which portions of material are removed or inserted before resealing the cuts via basic operations such as “climb” and “glide” [32–34]. Using lattice kirigami, one can create triangular or square patterns on the top surface of a 3D structure, as illustrated in Fig. 6(b). The triangles are on the top surfaces of the octahedra, while the squares are on the top surfaces of the cuboctahedra. These polyhedra interlock tightly, preventing any relative rotation of the triangles or squares. Although the lattice kirigami does not deform in plane, it indeed lifts the dimension of a flat surface.

The paradox of finite thickness and in-plane deformation from one piece of paper is addressed via a new approach called *folded kirigami*, which introduces folds and cuts to a flat surface and subsequently folds it into thick kirigami mechanisms [35]. Here, the dimension lifting is realized by rejoining faces, instead of resealing cuts. For a target kirigami pattern (e.g., the kagome pattern), an extended high-genus pattern is designed with appropriate sets of creases and cuts (Fig. 6(c), far left), and then folded to form the kirigami mechanism with finite thickness (Fig. 6(c), middle left). As a result, hinges perpendicular to the base triangles are created, allowing free in-plane rotation between the triangular prisms of the kagome folded kirigami. The fully deployed configuration with hexagonal holes and the fully retracted void-free configuration of the kagome folded kirigami are demonstrated in Fig. 6(c), middle left. This paradigm can also be used to make thick rotating-square mechanisms, as illustrated in Fig. 6(c), right. Moreover, the folded kirigami can be guided by explicit formulations that generate diverse irregular crease-cut patterns, including two representative mechanical metamaterial patterns of geometric and mechanical complexity: the transformable polarized kagome metamaterial and the nonreciprocal square-rhombus metamaterial, which will be discussed later. Importantly, the folded kirigami properly balance its in-plane stiffness and out-of-plane stiffness and strength—the folding hinges have quite low rotational stiffness so that the folded kirigami can be deployed and retracted easily as 2D mechanisms, and meanwhile, the cellular structures of the folded kirigami can sufficiently resist out-of-plane loading before large bending deformation or failure occurs. Such a combination of high *morphing efficiency* and high *flexural stiffness* is particularly useful in *robotic materials* [36,37].

3.3 Three-Dimensional Shape Morphing. Beyond shape morphing within a 2D surface (e.g., Fig. 2(b) and Figs. 3(g) and 3(h)), kirigami provides promising strategies for transforming surfaces in the 3D space. Such transformations can be categorized as follows: from one open surface to another open surface (Figs. 7(a) and 7(b)), from an open surface to a closed surface (Figs. 7(c) and 7(d)), and from one closed surface to another closed surface

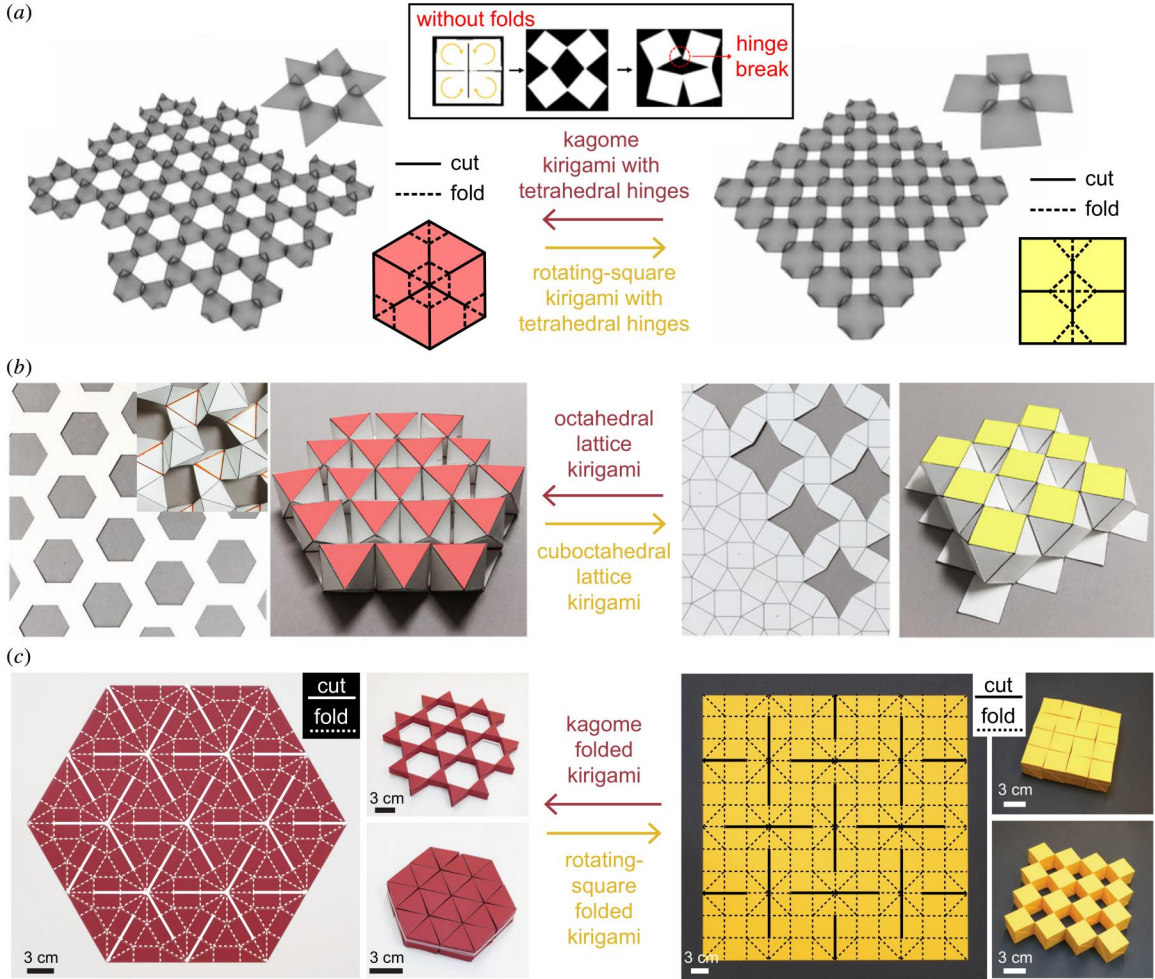


Fig. 6 Dimension lifting of kirigami with folds and cuts. (a) The kagome (left) and rotating square (right) kirigami with tetrahedral folding hinges [31]. The folding hinges allow free deployment and eliminate the out-of-plane buckling of the thin sheets. (b) The octahedral (left) and cuboctahedral (right) lattice kirigami can be constructed from one piece of paper with folds and holes [33]. The thick structures are interlocked tightly, prohibiting in-plane deformations. (c) The kagome (left) and rotating-square (right), made with the so-called “folded kirigami” approach, can be manufactured from a single piece of paper with both folds and cuts [35]. The thick mechanisms have perpendicular folding hinges, allowing nearly free in-plane deformations. Panel (a) is adapted with permission from Ref. [31], Copyright 2019 by the PNAS license. Panel (b) is adapted with permission from Ref. [33], Copyright 2016 by CC BY-NC 4.0 license. Panel (c) is adapted with permission from Ref. [35], Copyright 2024 by the Author(s).

(Figs. 7(e) and 7(f)). For all the examples illustrated in Fig. 7, the shape-morphing is geometry-dominated because the panel deformations are quite small compared to their rigid motions (i.e., rotations and translations) on the morphing path. The quadrilateral kirigami pattern in Fig. 7(a) is designed by matching the size and shape of the corresponding panels in the compact flat state and the deployed curved state, which are therefore geometrically compatible [5]. The pattern is bistable in theory but the prototype is monostable due to the significant rotational stiffness of the living hinges. The compatibility between the compact and the deployed kirigami surfaces can also be obtained in an indirect manner. For example, the conformal mapping from a target curved domain (Fig. 7(b), right) to a flat domain (Fig. 7(b), left) defines a locally isotropic scale factor that varies from one unit cell to another. By matching the scale factor and the expansion stiffness at each unit cell, one can transform the flat domain into the target curved domain [38]. This principle is implemented with the motif-inspired kirigami unit cell with a triangular core (Fig. 2(d), top left, and Fig. 7(b)). The unit cell provides isotropic auxetic expansion with tunable stiffness controlled by the size and orientation of the triangular core. The resulting kirigami pattern has an inhomogeneous cut distribution

(Fig. 7(b), left) and the prototype is stable at either the flat (Fig. 7(b), left) or the curved (Fig. 7(b), right) state.

Transformation from an open surface to a closed surface involves aligning properly designed open boundaries to “close” the shape. The aligning process can be realized from either a wrapping strategy [39–41] or a deploying strategy [42]. The wrapping strategy, for example, cuts a flat surface into multiple strips (Fig. 7(c), left) and seamlessly attaches them onto a base sphere (Fig. 7(c), right) [40]. The deploying strategy can be implemented by optimizing a free-form quadrilateral pattern (Fig. 7(d), left) to make it compatible with a deployed configuration fitting a target closed surface (Fig. 7(d), left) [42]. The quadrilateral pattern has considerable degrees-of-freedom upon 3D deployment, which enables it to deploy to a target shape of high complexity and even in topology.

A closed surface can be formed by sewing together the free boundaries of one or more open surfaces. In this context, morphing on a closed surface requires the synchronous evolution of its constituent units to maintain proper adjacency across the stitched boundaries, which imposes stricter constraints than morphing open surfaces individually. While the pure kirigami approach is efficacious in closing an open surface (Fig. 7(d)), the combination

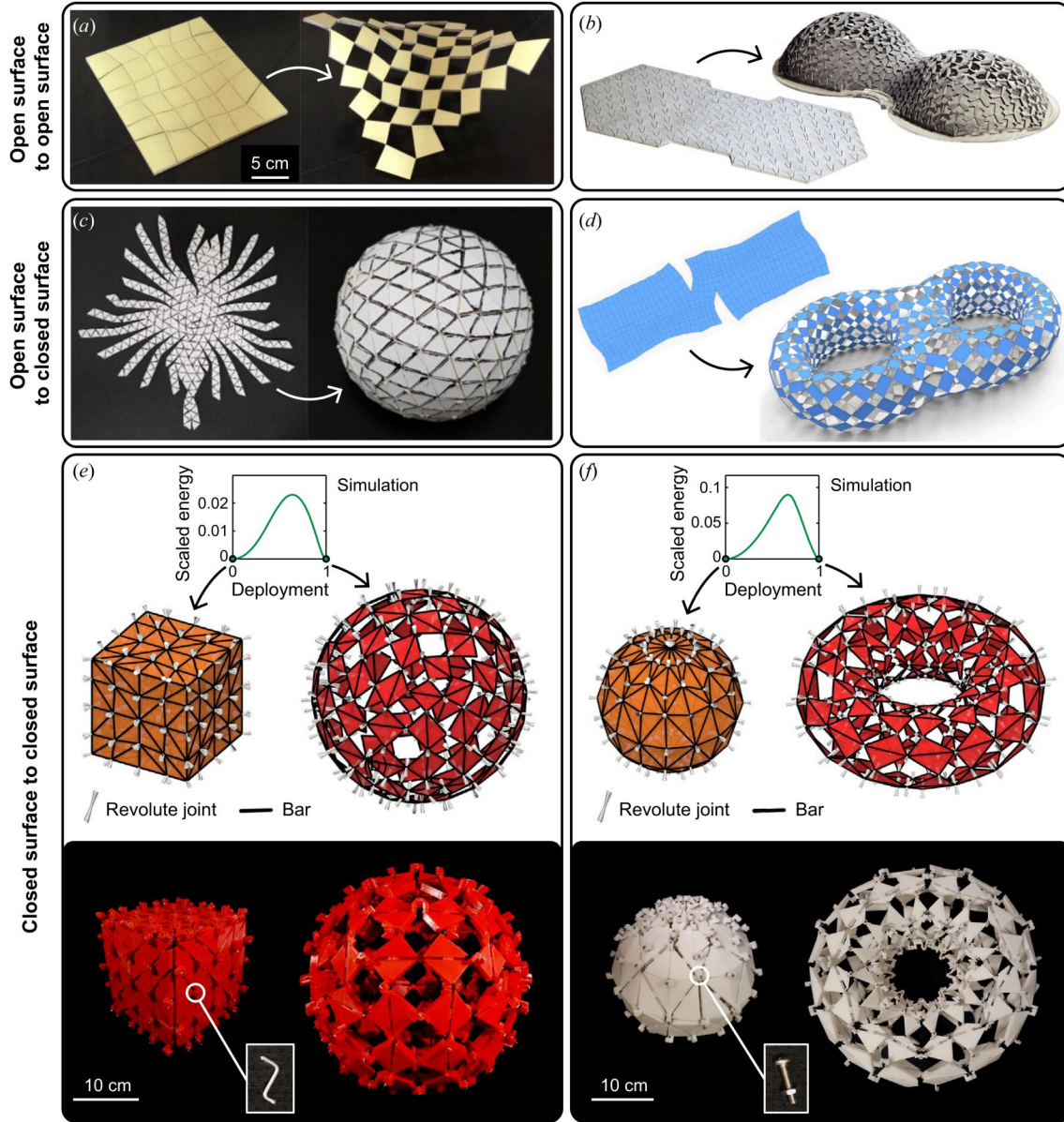


Fig. 7 Three-dimensional shape morphing of kirigami structures. (a) Monostable rubber sheet with a quadrilateral cutting pattern that expands to a hyperbolic paraboloid [5]. (b) Bistable rubber sheet with a motif-inspired cutting pattern that expands to an irregular surface with mixed curvature [38]. (c) Developable paper net that wraps a sphere [40]. (d) Quadrilateral kirigami pattern that deploys to a double torus [42]. (e) Bistable assemblage (top) and prototype (bottom) that deploys from a cube to a sphere [43]. The prototype was made by joining 3D-printed polylactic acid (PLA) panels with thin metal rods (inset). (f) Bistable assemblage (top) and prototype (bottom) that deploys from a sphere to a torus [43]. The prototype was made by joining 3D-printed PLA panels with thick screws and nuts (inset). In (e) and (f), the energy plots are from simulations with bar-and-hinge model. Panel (a) is adapted with permission from Ref. [5], Copyright 2019 by Springer Nature. Panel (b) is adapted with permission from Ref. [38], Copyright 2021 the Author(s). Panel (c) is adapted from Ref. [40], Copyright 2020 by CC BY-NC 4.0 license. Panel (d) is adapted with permission from Ref. [42], Copyright 2022 by Elsevier. Panels (e) and (f) are adapted with permission from Ref. [43], Copyright 2023 by CC BY-NC 4.0 license.

of cuts and folds enables controllable morphing between different closed surfaces with preserved topology (Fig. 7(e)) or changed topology (Fig. 7(f)) [43]. This combination facilitates precise morphing control by balancing flexibility and controllability—diagonal folds in quadrilateral panels allow finer curvature approximation with fewer panels, while revolute joints at cut intersections guide the bistable morphing process.

4 Mechanical Metamaterial Properties

Recently, the intersection of advanced physical systems and metamaterial design has led to the discovery of new classes of

mechanical metamaterials, for example, from topological insulators [44,45] to topological mechanical metamaterials [46–49], and from nonreciprocal optical or photonic devices [50,51] to nonreciprocal mechanical metamaterials [52–57]. Topological mechanical responses are attributable to the topology of phonon band structures of the metamaterials. Nonreciprocity breaks the transmission symmetry of a force between two points of the metamaterials. Interestingly, the topological and the nonreciprocal mechanical metamaterials have found their forms in locally isostatic lattices [58], as known as Maxwell lattices [59]: the kagome lattice for transformable topological mechanics [48] and the square-rhombus lattice for nonreciprocity [52]. In terms of geometric layouts, these

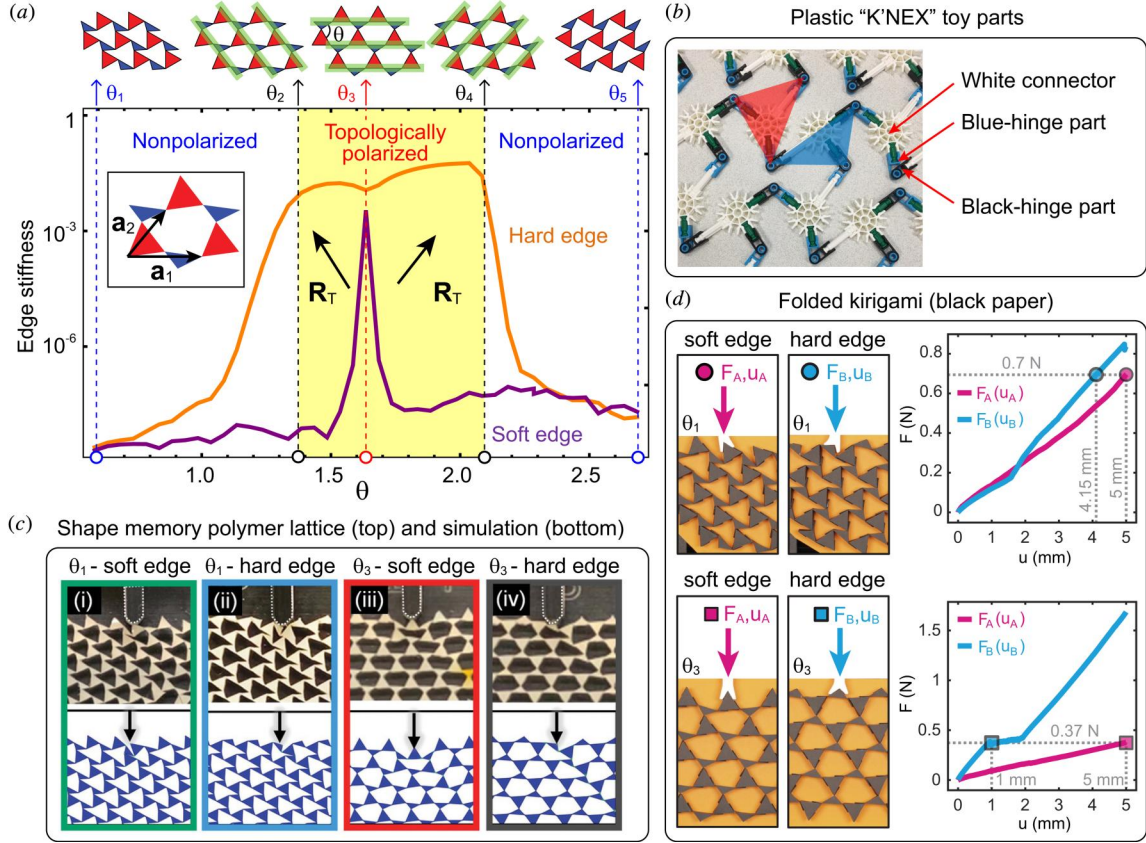


Fig. 8 Irregular kagome lattice and topological polarization transformation. (a) Soft and hard edge stiffness versus the twist angle θ of the irregular kagome lattice [48]. Five representative configurations (corresponding to θ_1 to θ_5) are shown. The twist angles θ_2 , θ_3 , and θ_4 define the critical configurations with collinear edges (highlighted by parallel strips). Across the critical configurations, the polarization vector R_T changes discontinuously. In the polarized regime (highlighted by shading), R_T points from the (bottom horizontal) hard edge to the (top horizontal) soft edge of the irregular kagome configurations above the graph. In the nonpolarized regime, $R_T=0$. (b) The irregular kagome prototype is assembled from plastic “K’NEX” parts [48]. (c) Snapshots of the indentation tests (top) and simulations (bottom) of the irregular kagome prototype made of shape memory polymers [64]. (d) Snapshots of the indentation tests of the irregular “folded kirigami” kagome lattice (left) and the experimental loading curves (right) [35]. In either (c) or (d), the indentation tests at the soft edge and the hard edge for one nonpolarized configuration (θ_1) and one polarized configuration (θ_3) are illustrated. Panels (a) and (b) are adapted from Ref. [48], Copyright 2017 by CC BY 4.0 license. Panel (c) is adapted from Ref. [64], Copyright 2023 by CC BY 4.0 license. Panel (d) is adapted with permission from Ref. [35], Copyright 2024 by Author(s).

2D hinged lattices can be seen as part of an emerging category of metamaterials—kirigami metamaterials, for which large deformations of 2D surfaces are programmed by the cuts [60].

4.1 Irregular Kagome Pattern and Topological Polarization Transformation. By breaking the symmetry of a regular kagome pattern (i.e., distorting equilateral triangles into scalene ones), the structure acquires the capacity to be *topologically polarized*, i.e., to push floppy modes from one edge to the other, causing no floppy mode at one edge and extra floppy modes at the opposite edge [48]. This polarization stems from phonon band topology of the pattern and therefore is robust against local geometric perturbations. In an irregular arrangement consisting of equilateral and scalene triangles, reconfiguring the pattern can toggle the appearance and disappearance of polarization, yielding *transformable topological mechanical metamaterials* [48]. Such *topological polarization transformation* can also be realized by combining two different scalene triangles [61]. In what follows, we describe the equilateral–scalene pattern in detail. As illustrated in Fig. 8(a), sweeping the twist angle θ applies uniform soft deformation to the irregular kagome pattern (or lattice in terms of physics) in its *Guest-Hutchinson mode* [62]. This uniform twisting transforms the pattern between polarized states ($\theta_2 < \theta < \theta_4$) and nonpolarized states ($\theta < \theta_2$ or $\theta > \theta_4$). The topological polarization \mathbf{R}_T is a Bravais

lattice vector that points toward the edge with extra floppy modes, expressed by [58,59]

$$\mathbf{R}_T = \sum_{i,j} n_j \mathbf{a}_i \quad (14)$$

in which \mathbf{a}_i are primitive vectors (Fig. 8(a), inset). The coefficients n_j are *integer topological invariants* of the equilibrium matrix $Q(\mathbf{k})$ for wavenumbers \mathbf{k} in the Brillouin zone, where the primitive reciprocal vectors \mathbf{b}_j satisfy $\mathbf{a}_i \cdot \mathbf{b}_j = 2\pi\delta_{ij}$. Specifically, n_j are *winding numbers* of the phase of $\det[Q(\mathbf{k})]$ around the cycles C_j connecting \mathbf{k} and $\mathbf{k} + \mathbf{b}_j$. They are expressed by [58,59]

$$n_j = \frac{1}{2\pi} \oint_{C_j} d\mathbf{k} \cdot \nabla_{\mathbf{k}} \phi(\mathbf{k}) \quad (15)$$

in which $\phi(\mathbf{k})$ is the phase of $\det[Q(\mathbf{k})]$. The winding numbers change only when θ crosses the *topological transitions* θ_2 , θ_3 , and θ_4 , resulting in distinct polarizations [48]

$$\mathbf{R}_T = \begin{cases} \mathbf{a}_2 - \mathbf{a}_1, & \theta_2 < \theta < \theta_3 \\ \mathbf{a}_2, & \theta_3 < \theta < \theta_4 \\ \mathbf{0}, & \theta < \theta_2 \text{ or } \theta > \theta_4 \end{cases} \quad (16)$$

The polarization vector \mathbf{R}_T cannot be well-defined at a transition, where bulk floppy modes (zero modes) arise. The zero modes are directly related to the lattice geometry that features collinear bonds (triangle edges). The collinear bonds generally allow states of self-stress, and furthermore, induce zero modes via the general Maxwell relation [58]

$$N_0 - N_{ss} = dN_s - N_b \quad (17)$$

which indicates that the number of zero modes N_0 and the number of states of self-stress N_{ss} vary synchronously if the number of sites N_s , the number of bonds N_b , and the dimension of the lattice d do not change. In nonpolarized states, floppy edge modes reside on both edges of the lattice. As θ sweeps from the nonpolarized regime to the polarized regime, the edge modes leave the bottom edge into the bulk, substantially increasing the bottom edge stiffness (i.e., the curve of hard edge in Fig. 8(a)), and become bulk floppy modes at the transitions. In polarized states, the edge modes gather at the edge pointed by \mathbf{R}_T . Notably, at the transition θ_3 , despite the appearance of a horizontal line of straight bonds supporting states of self-stress and a singular \mathbf{R}_T , the lattice still supports polarization in the vertical direction. This configuration is actually extensively used to produce topological polarization, such as in Refs. [35] and [63–65].

For physical realization of the topological polarization transformation, one has to consider the theoretical assumption that the triangles are connected by free hinges which facilitate the floppy edge modes as well as the uniform twisting in the Guest-Hutchinson mode. The original construction is the assembly of plastic modular buildings as illustrated in Fig. 8(b). The blue-hinge parts are inserted through the black-hinge parts, allowing free rotations between them. This assembly shows substantial change in the edge stiffness with the uniform twisting [48].

The topological polarization is also pursued with a single piece of material under the context of mechanical metamaterials, where living hinges take the place of ideal hinges [35,63–65]. The living hinges must have sufficiently low rotational stiffness to induce the polarization in the small deformation regime. Furthermore, the polarization transformation requires even much lower rotational stiffness—the hinges should maintain a low stress level after the uniform twisting, which involves large bending deformations of the hinges. To facilitate the polarization transformation, shape memory polymer is used to fabricate mechanical metamaterials of which the hinge stresses can be temporally erased (i.e., *stress caching*) under temperature control [64]. Such metamaterials can be stress-free in both the polarized and the nonpolarized configurations, avoiding stress accumulation in the hinges. As illustrated in Fig. 8(c), the shape memory polymer metamaterial exhibits significant edge stiffness change from its nonpolarized (i and ii) to its polarized configurations (iii and iv), with an agreement between simulation and experiment. Specifically, the hinge ligaments are 100 μm wide (versus maximum side length of 2.25 mm for the triangles) as an optimal compromise between their compliance and strength. Under this hinge size, the metamaterial exhibits a stiffness ratio of 2.18 between the hard and soft edges in the polarized state (θ_3) and of 1.15 in the nonpolarized state (θ_1), showcasing the polarization transformation.

Stronger polarization and transformation capability can be realized with one piece of paper by harnessing the extreme reconfigurability of the folded kirigami [35]. The folding hinges are almost ideal so that the reconfiguration of the folded kirigami is nearly stress-free. As illustrated in Fig. 8(d), the irregular kagome folded kirigami (paper thickness of 0.2 mm versus maximum triangle side length of 20 mm) exhibits a stiffness ratio of up to 5 in the polarized state (θ_3) and around 1.2 in the nonpolarized state (θ_1).

4.2 Square–Rhombus Pattern and Nonreciprocity. The Maxwell-Betti theorem indicates the static reciprocity of a linear elastic material undergoing infinitesimal strain—the displacement at a point (indexed by 2) induced by a force applied at another point (indexed by 1) equals the displacement at the point 1 induced by the

same force applied at the point 2 [66–68]. As illustrated in Fig. 9(a), an elementary example of reciprocal systems is a horizontal beam subjected to two vertical forces P_1 and P_2 at point 1 and point 2, respectively. We suppose Δ_{ij} is the displacement at point i induced by the force P_j , where $i,j = 1, 2$. Consider two states I and II of the beam. For state I, P_1 is applied first followed by P_2 . In this case, the total external work is expressed by

$$W_I = \frac{1}{2}P_1\Delta_{11} + \frac{1}{2}P_2\Delta_{22} + P_1\Delta_{12} \quad (18)$$

For state II, P_2 is applied first followed by P_1 . The total external work becomes

$$W_{II} = \frac{1}{2}P_2\Delta_{22} + \frac{1}{2}P_1\Delta_{11} + P_2\Delta_{21} \quad (19)$$

Under linear elasticity, the total external work is not affected by the order in which the forces are applied, i.e.,

$$W_I = W_{II} \quad (20)$$

Substituting Eqs. (18) and (19) into Eq. (20) yields

$$P_1\Delta_{12} = P_2\Delta_{21} \quad (21)$$

Supposing $P_1 = P_2 = P$, we have

$$\Delta_{12} = \Delta_{21} \quad (22)$$

Either Eqs. (21) or (22) expresses the concept of static reciprocity.

While breaking time-reversal symmetry or time-invariance of a media can generate nonreciprocity in linear elastic materials, spatial asymmetry, and nonlinearity are two necessary ingredients for static mechanical nonreciprocity [54]. Kirigami can provide both ingredients. Figure 9(b) illustrates a square-rhombus kirigami pattern, which is asymmetric regarding the left and right edges, quantified by the asymmetry angle $\theta = \pi/16$ [52]. Nonreciprocity emerges when a horizontal input force F_1 (or F_2) is applied on the middle point of the left (or right) edge. Under the same magnitude of the input force ($F_1 = F_2 = F$), the output displacement u_{21} (or u_{12}) on the right (or left) edge is different from each other. This discrepancy of “static transmissibility” in the opposite directions suggests the nonreciprocity of the kirigami system, expressed by

$$u_{12} \neq u_{21} \quad (23)$$

As illustrated in Fig. 9(c), substantial nonreciprocity can be detected from experiments and simulation, even for small input forces (i.e., $|F| \approx 0.2N$), indicating the strong nonlinearity of this system. Remarkably, the experimental curves from prototypes of different materials but the same size (squares of diagonal length 16 mm and rhombi of diagonal lengths 16 mm and 8 mm)—the silicon rubber (Fig. 9(d)) and the folded kirigami made of paper (Fig. 9(e))—approximately agree with each other and also match the simulation curve. This consistency highlights that the nonreciprocity of this kirigami system is controlled by its geometry, instead of the constituent materials. As motivated above, lack of reciprocity has the potential to be used as a design criterion in (quasi-)static mechanical systems and in other fields such as dynamics (nonreciprocity breaks the invariance when source and receiver are swapped), acoustics, and optics [69].

4.3 Rotating-Rectangle Pattern and Poisson’s Ratio.

Besides the emerging metamaterial functionalities such as the transformable polarization and the static nonreciprocity, kirigami is also employed to understand and design materials with negative Poisson’s ratio [70]. Two typical examples include the kagome pattern [71] and the rotating-square pattern [10], while more complex hybrid patterns can also be created [72]. For these kirigami

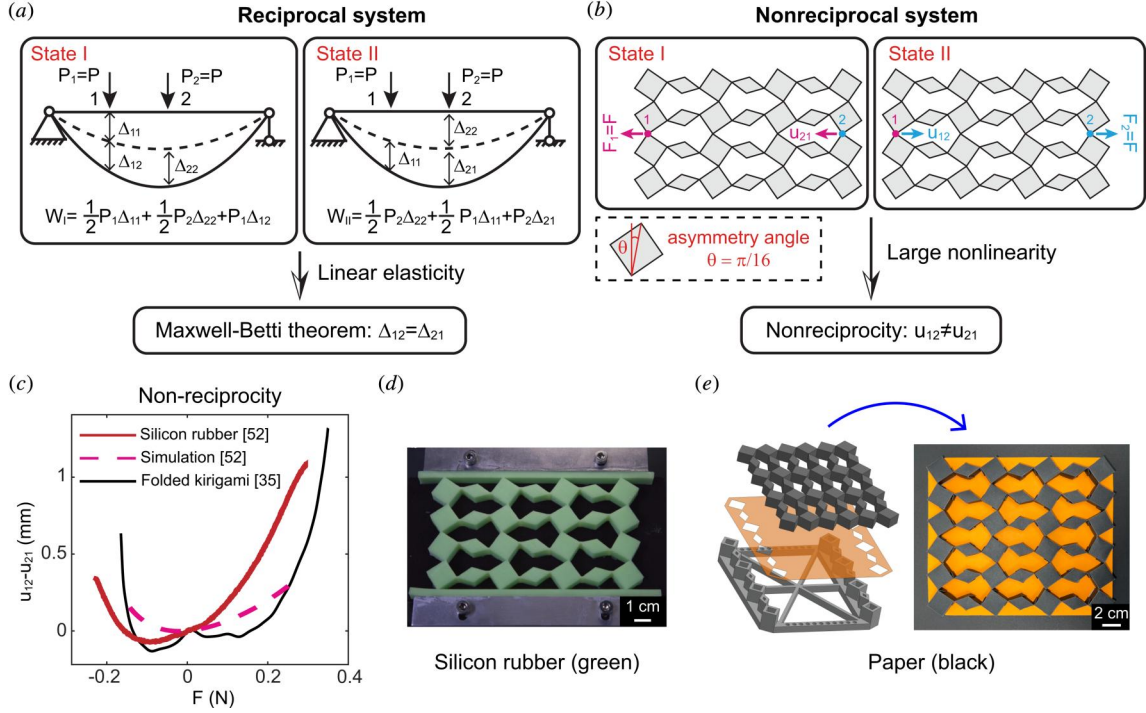


Fig. 9 Static nonreciprocity of the square-rhombus kirigami. (a) Concept of reciprocity is exemplified with a horizontal beam under vertical loadings. The force P_j is applied at the point j , causing the displacement Δ_{ij} at the point i ($i, j = 1, 2$). In state I, P_1 is applied first, followed by P_2 , resulting in the total external work W_I . In state II, P_2 is applied first, followed by P_1 , resulting in the total external work W_{II} . If the deformations are small, we have the reciprocal relationship $P_1\Delta_{12} = P_2\Delta_{21}$, which becomes $\Delta_{12} = \Delta_{21}$ when $P_1 = P_2 = P$. (b) The square-rhombus kirigami is nonreciprocal under the asymmetric angle $\theta = \pi/16$ [52]. The force F_j is applied at the point j , causing the displacement u_{ij} at the point i ($i, j = 1, 2$). The response is substantially nonlinear even for relatively small (but not too close to zero) input forces. Thus, we have the nonreciprocal relationship $F_1 u_{12} \neq F_2 u_{21}$, which becomes $u_{12} \neq u_{21}$ when $F_1 = F_2 = F$. (c) The nonreciprocity descriptor $u_{12} - u_{21}$ versus the input force $F_1 = F_2 = F$ [35,52]. The experimental curves are from the mechanical tests of (d) the silicon rubber prototype [52] and (e) the folded kirigami prototype [35]. Panel (d) is adapted with permission from Ref. [52], Copyright 2017 by Springer Nature. Panel (e) is adapted with permission from Ref. [35], Copyright 2024 by the Author(s).

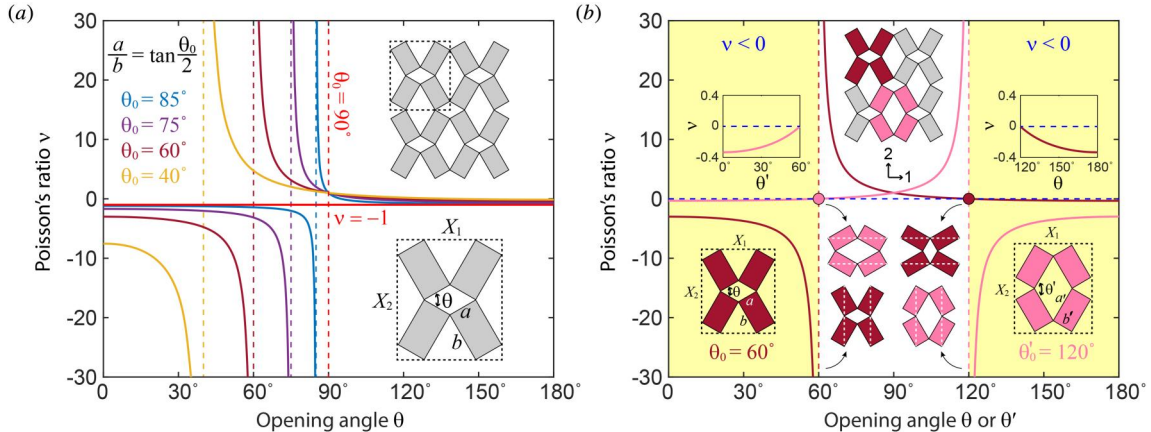


Fig. 10 Poisson's ratio v versus the rotation angle θ of rotating-rectangle kirigami [73]. The constituent rectangles have side lengths a and b . Four rectangles form a unit cell circumscribed within a large rectangle of side lengths X_1 and X_2 . (a) Curves for patterns with $a > b$. Each vertical dashed line corresponds to a critical angle θ_0 , which satisfies $a/b = \tan(\theta_0/2)$. The horizontal solid line ($v = -1$) corresponds to the degenerate (rotating-square) pattern with $a = b$. (b) Curves for two equivalent patterns under different parameterizations ($a > b$ and $a' < b'$). The parameters satisfy the following relationships: $a' = b$, $b' = a$, and $\theta' + \theta = 180^\circ$ deg.

patterns, the Poisson's ratio is governed purely by the geometry of their configurations. Here, we illustrate this phenomenon using the rotating-rectangle pattern (Fig. 10(a)) [73], which generalizes the classical rotating-square pattern. The rotating-rectangle patterns are composed of rectangles of side lengths a and b , and their

deformations are parameterized by a rotation angle θ . Extracting a unit cell of four rectangles, one obtains a circumscribed rectangle of side lengths X_1 and X_2 . To calculate the Poisson's ratio, one chooses a suitable strain measure, among various strain definitions such as the engineering strain, the infinitesimal strain, and the logarithmic

strain. While all these strain forms have their advantages and disadvantages in describing the deformations of a rotating-rectangle pattern [74], the infinitesimal strain—expressed by dX_1/X_1 and dX_2/X_2 for the two orthogonal directions 1 and 2, respectively—is more intrinsic because it does not rely on selecting a specific undeformed configuration. If the loading is applied in the direction 2, then the Poisson’s ratio is expressed by [73]

$$\nu = -\frac{dX_1/X_1}{dX_2/X_2} = \frac{a^2 \sin^2(\theta/2) - b^2 \cos^2(\theta/2)}{a^2 \cos^2(\theta/2) - b^2 \sin^2(\theta/2)} \quad (24)$$

For $a = b$, Eq. (24) indicates a constant Poisson’s ratio $\nu = -1$, which is corresponding to the rotating-square pattern. For $a \neq b$, ν is singular when the rotation angle θ equals

$$\theta_0 = 2 \arctan\left(\frac{a}{b}\right) \quad (25)$$

As illustrated in Fig. 10(b), a rotating-rectangle pattern with $a' > b'$ is equivalent to a rotating-rectangle pattern with $a < b$, under the relationships $a' = b$, $b' = a$, and $\theta' + \theta = 180$ deg. Therefore, only one case, say $a < b$, needs to be analyzed. Figure 10(a) shows that each curve of ν versus θ has two branches, separated by the vertical asymptote line $\theta = \theta_0$ and the horizontal line $\nu = -1$. Equation (25) indicates $\theta_0 < 90$ ° for $a < b$. On the left-hand side of the asymptote line ($\theta < \theta_0$), the Poisson’s ratio satisfies $\nu < -1$. As illustrated by the case of $a < b$ in Fig. 10(b), the singularity at the asymptote line arises because when $\theta = \theta_0$, the rectangle diagonals are collinear in the direction 2, resulting in $dX_2 = 0$. In addition, when the rotation angle θ equals

$$\theta'_0 = 180^\circ - \theta_0 = 2 \arctan\left(\frac{b}{a}\right) \quad (26)$$

the rectangle diagonals are collinear in the direction 1 (the case of $a < b$ in Fig. 10(b)). Therefore, we have $dX_1 = 0$ and consequently $\nu = 0$ for $\theta = \theta'_0$. On the right-hand side of this point ($\theta > \theta'_0$), the Poisson’s ratio satisfies $-1 < \nu < 0$, while on the left ($\theta_0 < \theta < \theta'_0$), we have $\nu > 0$. Desired values of the Poisson’s ratio can be obtained by selecting rotating-rectangle patterns with proper side lengths a and b and rotation angle θ .

By integrating rotating-square mechanisms with chiral origami modules, 3D metamaterials can undergo large, multimodal deformations that synchronize twisting and translation [75]. Since standard rotating-square patterns have a constant Poisson’s ratio, then generalized rotating-rectangle patterns may broaden the deformation modes of these 3D metamaterials with the feature of a tunable Poisson’s ratio.

5 Summary

This paper has focused on the underlying mechanism that transforms geometric characteristics of kirigami surfaces to their unique mechanical properties. The applications and challenges of kirigami engineering have been summarized in two recent reviews [76,77].¹ Their applications spread from flexible electronics to soft robotics, and from medical devices to energy and environmental devices. Their challenges include fabricating complex prototypes on small and large scales, balancing functional flexibility and structural integrity, and tailoring dynamics properties. We envision a couple of important directions for kirigami engineering regarding the interplay of geometry and mechanics: first, the theory of pattern design and deformation description of kirigami surfaces in general non-Euclidean space with varying curvatures; second, the fabrication strategy of kirigami surfaces with a proper material selection that

¹Although the term *kirigami engineering* is not present in these two contributions, they essentially discuss the same concept and put more emphasis on the application front.

minimizes the influence of local constituent material properties on the global mechanical responses predicted by the geometric analysis. Kirigami expands the design space and offers an effective toolkit for engineering and scientific applications involving the interplay of geometry and mechanics. It allows creative designs that are not only aesthetically compelling but also mechanically ingenious.

Acknowledgment

The authors thank Stefano Gonella, Isabel Moreira de-Oliveira, Yifan Rao, Yifan Wang, Shixi Zang, and Audrey Zhang for helpful discussions.

References

- [1] Misseroni, D., Pratapa, P. P., Liu, K., Kresling, B., Chen, Y., Darai, C., and Paulino, G. H., 2024, “Origami Engineering,” *Nat. Rev. Methods Primers*, **4**(1), p. 40.
- [2] Zhao, Y., Liang, Q., Li, S., Chen, Y., Liu, X., Sun, H., Wang, C., Ji, C.-Y., Li, J., and Wang, Y., 2024, “Thermal Emission Manipulation Enabled by Nano-Kirigami Structures,” *Small*, **20**(3), p. 2305171.
- [3] Han, D., Li, W., Liu, M., Sun, T., Hou, Y., Chen, X., Shi, H., et al., 2023, “Kirigami-Inspired Planar Deformable Metamaterials for Multiple Dynamic Electromagnetic Manipulations,” *Laser Photonics Rev.*, **17**(11), p. 2300374.
- [4] Choi, G. P., Dudte, L. H., and Mahadevan, L., 2021, “Compact Reconfigurable Kirigami,” *Phys. Rev. Res.*, **3**(4), p. 043030.
- [5] Choi, G. P., Dudte, L. H., and Mahadevan, L., 2019, “Programming Shape Using Kirigami Tessellations,” *Nat. Mater.*, **18**(9), pp. 999–1004.
- [6] Rafsanjani, A., and Pasini, D., 2016, “Bistable Auxetic Mechanical Metamaterials Inspired by Ancient Geometric Motifs,” *Ext. Mech. Lett.*, **9**(2), pp. 291–296.
- [7] Qiao, C., Agnelli, F., Pokkalla, D. K., D’Ambrosio, N., and Pasini, D., 2024, “Anisotropic Morphing in Bistable Kirigami Through Symmetry Breaking and Geometric Frustration,” *Adv. Mater.*, **36**(23), p. 2313198.
- [8] Meeuissen, A., Corvi, A., and Bertoldi, K., 2025, “A New Design Strategy for Highly Multistable Kirigami Metamaterials,” *Adv. Funct. Mater.*, **35**(19), p. 2421638.
- [9] Qiao, C., Chen, S., Chen, Y., Zhou, Z., Jiang, W., Wang, Q., Tian, X., and Pasini, D., 2025, “Inverse Design of Kirigami Through Shape Programming of Rotating Units,” *Phys. Rev. Lett.*, **134**(17), p. 176103.
- [10] Grima, J. N., and Evans, K. E., 2000, “Auxetic Behavior From Rotating Squares,” *J. Mater. Sci. Lett.*, **19**(17), pp. 1563–1565.
- [11] Dang, X., Feng, F., Duan, H., and Wang, J., 2021, “Theorem for the Design of Deployable Kirigami Tessellations With Different Topologies,” *Phys. Rev. E*, **104**(5), p. 055006.
- [12] Dudte, L. H., Choi, G. P., Becker, K. P., and Mahadevan, L., 2023, “An Additive Framework for Kirigami Design,” *Nat. Comput. Sci.*, **3**(5), pp. 443–454.
- [13] Dang, X., Feng, F., Duan, H., and Wang, J., 2022, “Theorem on the Compatibility of Spherical Kirigami Tessellations,” *Phys. Rev. Lett.*, **128**(3), p. 035501.
- [14] Jin, L., Forte, A. E., Deng, B., Rafsanjani, A., and Bertoldi, K., 2020, “Kirigami-Inspired Inflatables With Programmable Shapes,” *Adv. Mater.*, **32**(33), p. 2001863.
- [15] Radaelli, P. G., 2011, “Wallpaper (Plane) Groups,” *Symmetry in Crystallography: Understanding the International Tables*, Oxford University Press, New York.
- [16] Liu, L., Choi, G. P., and Mahadevan, L., 2021, “Wallpaper Group Kirigami,” *Proc. R. Soc. A*, **477**(2252), p. 20210161.
- [17] Liu, L., Choi, G. P., and Mahadevan, L., 2022, “Quasicrystal Kirigami,” *Phys. Rev. Res.*, **4**(3), p. 033114.
- [18] Rafsanjani, A., and Bertoldi, K., 2017, “Buckling-Induced Kirigami,” *Phys. Rev. Lett.*, **118**(8), p. 084301.
- [19] Blees, M. K., Barnard, A. W., Rose, P. A., Roberts, S. P., McGill, K. L., Huang, P. Y., Ruyack, A. R., et al., 2015, “Graphene Kirigami,” *Nature*, **524**(7564), pp. 204–207.
- [20] Lamoureux, A., Lee, K., Shlian, M., Forrest, S. R., and Shtein, M., 2015, “Dynamic Kirigami Structures for Integrated Solar Tracking,” *Nat. Commun.*, **6**(1), p. 8092.
- [21] Chen, Y., He, R., Hu, S., Zeng, Z., Guo, T., Feng, J., and Sareh, P., 2024, “Design-Material Transition Threshold of Ribbon Kirigami,” *Mater. Des.*, **242**, p. 112979.
- [22] Yang, Y., Dias, M. A., and Holmes, D. P., 2018, “Multistable Kirigami for Tunable Architected Materials,” *Phys. Rev. Mater.*, **2**(11), p. 110601.
- [23] Zhang, Y., Yan, Z., Nan, K., Xiao, D., Liu, Y., Luan, H., Fu, H., et al., 2015, “A Mechanically Driven Form of Kirigami as a Route to 3D Mesostructures in Micro/Nanomembranes,” *Proc. Natl. Acad. Sci.*, **112**(38), pp. 11757–11764.
- [24] Yan, Z., Zhang, F., Liu, F., Han, M., Ou, D., Liu, Y., Lin, Q., et al., 2016, “Mechanical Assembly of Complex, 3D Mesostructures From Releasable Multilayers of Advanced Materials,” *Sci. Adv.*, **2**(9), p. e1601014.
- [25] Yan, Z., Zhang, F., Wang, J., Liu, F., Guo, X., Nan, K., Lin, Q., et al., 2016, “Controlled Mechanical Buckling for Origami-Inspired Construction of 3D Microstructures in Advanced Materials,” *Adv. Funct. Mater.*, **26**(16), pp. 2629–2639.
- [26] Zhang, Q., Pan, N., Liu, S., Feng, J., and Cai, J., 2024, “Self-Locking Kirigami Surfaces Via Controlled Stretching,” *Commun. Eng.*, **3**(1), p. 26.

- [27] de Oliveira, I. M., Sosa, E. M., Baker, E., and Adriaenssens, S., 2023, "Experimental and Numerical Investigation of a Rotational Kirigami System," *Thin-Walled Struct.*, **192**, p. 111123.
- [28] Liu, Z., Du, H., Li, J., Lu, L., Li, Z.-Y., and Fang, N. X., 2018, "Nano-Kirigami With Giant Optical Chirality," *Sci. Adv.*, **4**(7), p. eaat4436.
- [29] Wu, L., and Pasini, D., 2024, "Zero Modes Activation to Reconcile Floppiness, Rigidity, and Multistability Into an All-in-One Class of Reprogrammable Metamaterials," *Nat. Commun.*, **15**(1), p. 3087.
- [30] Meeussen, A. S., Bordiga, G., Chang, A. X., Spoettling, B., Becker, K. P., Mahadevan, L., and Bertoldi, K., 2025, "Textile Hinges Enable Extreme Properties of Kirigami Metamaterials," *Adv. Funct. Mater.*, **35**(9), p. 2415986.
- [31] Tang, Y., Li, Y., Hong, Y., Yang, S., and Yin, J., 2019, "Programmable Active Kirigami Metasheets With More Freedom of Actuation," *Proc. Natl. Acad. Sci.*, **116**(52), pp. 26407–26413.
- [32] Castle, T., Cho, Y., Gong, X., Jung, E., Sussman, D. M., Yang, S., and Kamien, R. D., 2014, "Making the Cut: Lattice Kirigami Rules," *Phys. Rev. Lett.*, **113**(24), p. 245502.
- [33] Castle, T., Sussman, D. M., Tanis, M., and Kamien, R. D., 2016, "Additive Lattice Kirigami," *Sci. Adv.*, **2**(9), p. e1601258.
- [34] Sussman, D. M., Cho, Y., Castle, T., Gong, X., Jung, E., Yang, S., and Kamien, R. D., 2015, "Algorithmic Lattice Kirigami: A Route to Pluripotent Materials," *Proc. Natl. Acad. Sci.*, **112**(24), pp. 7449–7453.
- [35] Dang, X., Gonella, S., and Paulino, G. H., 2024, "Folding a Single High-Genus Surface Into a Repertoire of Metamaterial Functionalities," *Proc. Natl. Acad. Sci.*, **121**(46), p. e2413370121.
- [36] Hannard, F., Mirkhalaf, M., Ameri, A., and Barthelat, F., 2021, "Segmentations in Fins Enable Large Morphing Amplitudes Combined With High Flexural Stiffness for Fish-Inspired Robotic Materials," *Sci. Rob.*, **6**(57), p. eabf9710.
- [37] Chen, T., Yang, X., Zhang, B., Li, J., Pan, J., and Wang, Y., 2024, "Scale-Inspired Programmable Robotic Structures With Concurrent Shape Morphing and Stiffness Variation," *Sci. Rob.*, **9**(92), p. eadl0307.
- [38] Chen, T., Panetta, J., Schnaubelt, M., and Pauly, M., 2021, "Bistable Auxetic Surface Structures," *ACM Trans. Graph.*, **40**(4), pp. 1–9.
- [39] Abdullah, A. M., Li, X., Braun, P. V., Rogers, J. A., and Hsia, K. J., 2020, "Kirigami-Inspired Self-Assembly of 3D Structures," *Adv. Funct. Mater.*, **30**(14), p. 1909888.
- [40] Lee, Y.-K., Xi, Z., Lee, Y.-J., Kim, Y.-H., Hao, Y., Choi, H., Lee, M.-G., et al., 2020, "Computational Wrapping: A Universal Method to Wrap 3D-Curved Surfaces With Nonstretchable Materials for Conformal Devices," *Sci. Adv.*, **6**(15), p. eaax6212.
- [41] Yang, X., Liu, M., Zhang, B., Wang, Z., Chen, T., Zhou, Y., Chen, Y., Hsia, K. J., and Wang, Y., 2024, "Hierarchical Tessellation Enables Programmable Morphing Matter," *Matter*, **7**(2), pp. 603–619.
- [42] Jiang, C., Rist, F., Wang, H., Wallner, J., and Pottmann, H., 2022, "Shape-Morphing Mechanical Metamaterials," *Comput.-Aided Des.*, **143**, p. 103146.
- [43] Dang, X., Chen, S., Acha, A. E., Wu, L., and Pasini, D., 2025, "Shape and Topology Morphing of Closed Surfaces Integrating Origami and Kirigami," *Sci. Adv.*, **11**(18), p. eads5659.
- [44] Hasan, M. Z., and Kane, C. L., 2010, "Colloquium: Topological Insulators," *Rev. Mod. Phys.*, **82**(4), pp. 3045–3067.
- [45] Qi, X.-L., and Zhang, S.-C., 2011, "Topological Insulators and Superconductors," *Rev. Mod. Phys.*, **83**(4), pp. 1057–1110.
- [46] Nash, L. M., Kleckner, D., Read, A., Vitelli, V., Turner, A. M., and Irvine, W. T., 2015, "Topological Mechanics of Gyroscopic Metamaterials," *Proc. Natl. Acad. Sci.*, **112**(47), pp. 14495–14500.
- [47] Chen, B. G.-G., Liu, B., Evans, A. A., Paulose, J., Cohen, I., Vitelli, V., and Santangelo, C. D., 2016, "Topological Mechanics of Origami and Kirigami," *Phys. Rev. Lett.*, **116**(13), p. 135501.
- [48] Rocklin, D. Z., Zhou, S., Sun, K., and Mao, X., 2017, "Transformable Topological Mechanical Metamaterials," *Nat. Commun.*, **8**(1), p. 14201.
- [49] Liu, B., Silverberg, J. L., Evans, A. A., Santangelo, C. D., Lang, R. J., Hull, T. C., and Cohen, I., 2018, "Topological Kinematics of Origami Metamaterials," *Nat. Phys.*, **14**(8), pp. 811–815.
- [50] Lira, H., Yu, Z., Fan, S., and Lipson, M., 2012, "Electrically Driven Nonreciprocity Induced by Interband Photonic Transition on a Silicon Chip," *Phys. Rev. Lett.*, **109**(3), p. 033901.
- [51] Fleury, R., Sounas, D. L., Sieck, C. F., Haberman, M. R., and Alù, A., 2014, "Sound Isolation and Giant Linear Nonreciprocity in a Compact Acoustic Circulator," *Science*, **343**(6170), pp. 516–519.
- [52] Coulais, C., Sounas, D., and Alù, A., 2017, "Static Non-Reciprocity in Mechanical Metamaterials," *Nature*, **542**(7642), pp. 461–464.
- [53] Brandenbourger, M., Locsin, X., Lerner, E., and Coulais, C., 2019, "Non-Reciprocal Robotic Metamaterials," *Nat. Commun.*, **10**(1), p. 4608.
- [54] Nassar, H., Yousefzadeh, B., Fleury, R., Ruzzene, M., Alù, A., Daraio, C., Norris, A. N., Huang, G., and Haberman, M. R., 2020, "Nonreciprocity in Acoustic and Elastic Materials," *Nat. Rev. Mater.*, **5**(9), pp. 667–685.
- [55] Wang, X., Li, Z., Wang, S., Sano, K., Sun, Z., Shao, Z., Takeishi, A., et al., 2023, "Mechanical Nonreciprocity in a Uniform Composite Material," *Science*, **380**(6641), pp. 192–198.
- [56] Zhan, J., Qiu, X., and Hou, H., 2023, "Engineering Mechanical Nonreciprocity in Homogeneous Materials: From Biomimetic to Bioapplications," *Mater.*, **6**(8), pp. 2608–2610.
- [57] Veenstra, J., Gamayun, O., Guo, X., Sarvi, A., Meinersen, C. V., and Coulais, C., 2024, "Non-Reciprocal Topological Solitons in Active Metamaterials," *Nature*, **627**(8004), pp. 528–533.
- [58] Kane, C. L., and Lubensky, T. C., 2014, "Topological Boundary Modes in Isostatic Lattices," *Nat. Phys.*, **10**(1), pp. 39–45.
- [59] Lubensky, T., Kane, C., Mao, X., Souslov, A., and Sun, K., 2015, "Phonons and Elasticity in Critically Coordinated Lattices," *Rep. Prog. Phys.*, **78**(7), p. 073901.
- [60] Zhai, Z., Wu, L., and Jiang, H., 2021, "Mechanical Metamaterials Based on Origami and Kirigami," *Appl. Phys. Rev.*, **8**(4), p. 041319.
- [61] Xiu, H., Liu, H., Poli, A., Wan, G., Sun, K., Arruda, E. M., Mao, X., and Chen, Z., 2022, "Topological Transformability and Reprogrammability of Multistable Mechanical Metamaterials," *Proc. Natl. Acad. Sci.*, **119**(52), p. e2211725119.
- [62] Guest, S. D., and Hutchinson, J. W., 2003, "On the Determinacy of Repetitive Structures," *J. Mech. Phys. Solids*, **51**(3), pp. 383–391.
- [63] Pishvar, M., and Harne, R. L., 2020, "Soft Topological Metamaterials With Pronounced Polar Elasticity in Mechanical and Dynamic Behaviors," *Phys. Rev. Appl.*, **14**(4), p. 044034.
- [64] Jolly, J. C., Jin, B., Jin, L., Lee, Y., Xie, T., Gonella, S., Sun, K., Mao, X., and Yang, S., 2023, "Soft Mechanical Metamaterials With Transformable Topology Protected by Stress Caching," *Adv. Sci.*, **10**(22), p. 2302475.
- [65] Iorio, L., Ardito, R., and Gonella, S., 2024, "Edge-Selective Reconfiguration in Polarized Lattices With Magnet-Enabled Bistability," *Ext. Mech. Lett.*, **7**(1), p. 102217.
- [66] Maxwell, J. C., 1864, "On the Calculation of the Equilibrium and Stiffness of Frames," *London, Edinburgh, Dublin Philos. Mag. J. Sci.*, **27**(182), pp. 294–299.
- [67] Betti, E., 1872, "Teoria Della Elasticita," *Il Nuovo Cimento (1869-1876)*, **7**(1), pp. 69–97.
- [68] Charlton, T., 1960, "A Historical Note on the Reciprocal Theorem and Theory of Statically Indeterminate Frameworks," *Nature*, **187**(4733), pp. 231–232.
- [69] Bordiga, G., Piccolroaz, A., and Bigoni, D., 2022, "A Way to Hypo-Elastic Artificial Materials Without a Strain Potential and Displaying Flutter Instability," *J. Mech. Phys. Solids*, **158**, p. 104665.
- [70] Saxena, K. K., Das, R., and Calius, E. P., 2016, "Three Decades of Auxetics Research – Materials With Negative Poisson's Ratio: A Review," *Adv. Eng. Mater.*, **18**(11), pp. 1847–1870.
- [71] Grima, J., Alderson, A., and Evans, K., 2005, "An Alternative Explanation for the Negative Poisson's Ratios in Auxetic Foams," *J. Phys. Soc. Jpn.*, **74**(4), pp. 1341–1342.
- [72] Lim, T.-C., 2024, "A Mechanical Metamaterial With Adjustable Positive to Negative Poisson's Ratio Based on Rotating Trapeziums and Triangles," *Philos. Mag.*, **104**(5), pp. 300–320.
- [73] Grima, J., Alderson, A., and Evans, K., 2004, "Negative Poisson's Ratios From Rotating Rectangles," *Comput. Methods Sci. Technol.*, **10**(2), pp. 137–145.
- [74] Grima-Cornish, J. N., Grima, J. N., and Attard, D., 2021, "Mathematical Modeling of Auxetic Systems: Bridging the Gap Between Analytical Models and Observation," *Int. J. Mech. Mater. Eng.*, **16**(1), pp. 1–22.
- [75] Zhao, T., Dang, X., Manos, K., Zang, S., Mandal, J., Chen, M., and Paulino, G. H., 2025, "Modular Chiral Origami Metamaterials," *Nature*, **640**(8060), pp. 931–940.
- [76] Tao, J., Khosravi, H., Deshpande, V., and Li, S., 2023, "Engineering by Cuts: How Kirigami Principle Enables Unique Mechanical Properties and Functionalities," *Adv. Sci.*, **10**(1), p. 2204733.
- [77] Jin, L., and Yang, S., 2024, "Engineering Kirigami Frameworks Toward Real-World Applications," *Adv. Mater.*, **36**(9), p. 2308560.